An Adaptive Neuro-Fuzzy Controller for Vibration Suppression of

a Flexible Structure in Aerial Refueling

by

Adam Genno

Submitted in partial fulfillment of the requirements for the

degree of Master of Science in Mechanical Engineering

Lakehead University

Thunder Bay, Ontario

September 2022

Abstract

Air-to-air refueling (AAR) has been commonly used in military jet applications. Recently, civilian applications of AAR have been garnering increased attention due to the high cost of air travel, which is largely dictated by the cost of jet fuel. There are two types of AAR approaches: probe-drogue and flying boom systems. This work explores the probe-drogue AAR system in commercial applications. Typical AAR applications deploy a drogue connected to a long flexible hose behind a moving aircraft tanker. The drogue is connected to a probe in a receiver aircraft before initiating fuel transfer and is retracted back into the tanker when the fuel transfer is completed. In order to ensure a safe and efficient refueling operation sophisticated systems need to be developed to accommodate the turbulences encountered, particularly in respect to vibration reduction of the flexible hose and drogue. The objective of this work is to develop a probe-drogue system for helicopter AAR applications. The first project is to make a preliminary design of a new AAR system for helicopter refuelling from a modified AT-802 tanker aircraft.

The second project is to model and control the drogue system under different turbulence conditions. As the real AAR system is not available, a flexible structure will be used instead to explore strategies for adaptive drogue system control. In order to achieve adaptive control of the flexible structure, an adaptive neuro-fuzzy (NF) controller is developed to suppress the vibration of perturbed flexible structures under variable dynamics conditions. A new hybrid training technique based on the bisection particle swarm optimization (BPSO) algorithm is proposed to optimize the NF controller parameters recursively to accommodate changes to system dynamics. To solve the issue of controller response to nonlinearities inducing additional vibrations in the steady state solution space, a fuzzy boundary function is proposed to shape the control signal output. The parameters related to output suppression are optimized simultaneously during recursive NF system training. The effectiveness of the proposed NF controller and hybrid training method is verified by experimental tests under different system dynamics conditions by placing mass blocks at different locations on the flexible beam. Experimental tests have shown that the proposed adaptive NF controller and hybrid training method outperform other related control schemes in terms of overshoot, undershoot, and settling time.

Acknowledgements

Table of Contents

List of Figures

List of Tables

List of Symbols

Symbol	Meaning
$D_{h,i}$	Internal diameter of refueling hose
$D_{h,o}$	External diameter of refueling hose
D_s	Hose drum spool diameter
$L_{h,d}$	Desired length of refueling hose
L_s	Hose drum spool length
PF	Packing factor
$\ddot{\theta}, \alpha$	Angular acceleration
$\dot{\theta}, \omega$	Angular velocity
m_1, m_2, m_3	Point mass
W	Weight
θ_1, θ_2	Pendulum link angle
ℓ_1, ℓ_2	Length of pendulum link
V	Voltage
A	Amperage
m_b	Motor structure mass
ℓ_p	Length of pendulum arm
m_p	Pendulum mass
θ_p	Angular position of the pendulum arm
$\dot{\theta}_p$	Angular velocity of the pendulum arm
m_a	Additional mass block
k_s	Spring constant
ℓ_b	Length of flexible beam
x_b	Deflection of flexible beam
$\dot{x}_b$	Deflection velocity of flexible beam
g	Gravity constant
P	Potential energy
V	Total potential energy

K	Kinetic energy
T	Total kinetic energy
J_p	Mass moment of inertia
x	General term for position
$v, \dot{x}$	General term for velocity
$\omega, \dot{\theta}$	General term for angular velocity
r	General term for radius
L	Lagrangian
$q, \dot{q}$	Generalized coordinates position
Q	Generalized force
τ	Torque
B_b	Flexible beam viscous friction torque coefficient
B_p	Pendulum viscous friction torque coefficient
η_g	Gearbox efficiency
K_g	Total gearbox ratio
η_m	Motor efficiency
k_t	Motor torque constant
V_m	Motor input voltage
k_m	Back-emf constant
R_m	Motor armature resistance
u	Generalized control signal
$k_{p,x}$	Proportional control term for deflection
$k_{p,\theta}$	Proportional control term for angular position
$k_{d,x}$	Derivative control term for deflection velocity
$k_{d,\theta}$	Derivative control term for angular velocity
$\boldsymbol{q}$	Vector containing state-space variables
$\boldsymbol{A}, \boldsymbol{B}, \boldsymbol{C}, \boldsymbol{D}$	State-space matrices
$\boldsymbol{Q}, \boldsymbol{R}$	LQR weighting matrices
H	Butterworth filter
ω_{cf}	Cutoff frequency

ω_n	Natural frequency
$\mathcal{R}_j$	Fuzzy rule
z	Neuro-fuzzy control output
A_i^g	Neuro-fuzzy membership function
μ_n	Neuro-fuzzy membership function output
a_J, c_J	Nonlinear neuro-fuzzy membership function
w_j	Fuzzy rule firing strength
N_j	Normalized firing strength
p_j, q_j, r_j, s_j, t_j	Linear neuro-fuzzy parameters
$\mathcal{B}_u$	Upper BPSO boundary particle
$\mathcal{B}_l$	Lower BPSO boundary particle
δ	Half the width of the initial BPSO solution space
b	Generalized variable
γ	Percentage parameter
ε_u	Error of upper BPSO particle
ε_l	Error of lower BPSO particle
y_u	NF controller output with upper BPSO parameters
y_l	NF controller output with lower BPSO parameters
y	NF controller output
ε_{min}	Stopping criterion
$\boldsymbol{u}$	Vector containing NF controller inputs
$\boldsymbol{\theta}$	Vector containing linear NF controller parameters
f	Nodal outputs from Layer 4 of the NF controller
$E(\boldsymbol{\theta})$	Objective (error) function
c_v	Viscous damping coefficient
f_r	Restoring force
λ	Damping ratio parameter
σ	Parameter for the standard deviation of a Gaussian MF
c	Parameter for the center of a Gaussian MF

List of Abbreviations

Abbreviation	Meaning
3-DOF	Three degrees of freedom
3D	Three dimensional
AAR	Air-to-air refueling
AC	Adaptive control
ANFIS	Adaptive neuro-fuzzy inference system
BPSO	Bisection particle swarm optimization
CG	Center of gravity
DAQ	Data acquisition
DC	Direct current
DSC	Dynamic surface control
FL	Fuzzy logic
GD	Gradient descent
LQR	Linear-quadratic-regulator
LSE	Least-squares estimator
MF	Membership function
NASA	National Aeronautics and Space Administration
NATO	North Atlantic Treaty Organization
NF	Neuro-fuzzy
NN	Neural network
PD	Proportional-derivative
PI	Proportional-integral
PID	Proportional-integral-derivative
SMC	Sliding mode control
STANAG	Standard agreement
ZN	Ziegler-Nichols

Chapter 1

Introduction

1.1 Research Motivation

Air-to-air refueling (AAR) is used to significantly extend the effective range of an aircraft by performing refueling operations mid-flight. There are several strategic advantages to AAR. 1) It allows an aircraft to perform takeoff with less fuel in place of a greater payload, such as additional personnel and armaments; 2) it allows several consecutive operations to be performed by a receiver aircraft, and a tanker aircraft can refuel multiple receiver aircraft several times. The two main approaches used to perform AAR are flying-boom and probe-drogue systems, each of which has specific merits and limitations. As shown in Figure 1.1, a flying-boom system utilizes a rigid telescoping structure that is extended into a receiver aircraft, while a probe-drogue system extends a drogue canopy attached to a flexible hose behind a tanker aircraft. The drogue canopy stabilizes the flexible hose and provides a target for the pilot of the receiver aircraft, who navigates a probe into the drogue to initiate AAR.

(a)

(b)

Figure 1.1: AAR systems: (a) flying boom [1], (b) probe-drogue [2].

The flying-boom approach was originally designed to refuel larger, less maneuverable aircrafts and allows for larger refueling rates compared to probe-drogue systems; but it requires the receiver aircraft to be in close proximity to the tanker aircraft [3]. A probe-drogue system is typically contained within a dedicated refuelling pod and is more flexible as a result. Multiple probe-drogue refuelling pods can be installed on an aircraft to allow for the refueling of multiple aircrafts simultaneously, as shown in Figure 1.2. Recently, the Royal Canadian Air Force (RCAF) utilized a probe-drogue equipped Airbus CC-150 Polaris to support the Global Coalition in Iraq and Syria as a part of Operation IMPACT. From 2014 to 2019, this aircraft supported Coalition air operations 365 days a year, flying a total of 1166 sorties and delivering over 65 million pounds of fuel [4]. An example is shown in Figure 1.1(b); it uses the probe-drogue AAR of a Boeing EA-18G Growler, which is a specialized version of the F/A-18F Super Hornet used for electronics warfare. The AAR provided by the RCAF Airbus CC-150 Polaris allowed this aircraft to perform four consecutive missions during Operation IMPACT.

Figure 1.2: Flight demo showcasing the aerial refueling of the RCAF Airbus CC-150 Polaris at AirShow London 2020 [5].

Probe-drogue systems are commonly used in military AAR applications to connect a tanker aircraft to a receiver aircraft [6, 7]. However, AAR technology has not yet been applied to commercial applications due to significant variations in operating conditions [8, 9]. From an operational concept perspective, AAR-based models have been proposed to help reduce the environmental impact and improve the fuel efficiency of long-haul flights [10]. Similarly, simulations in [11] estimate a reduction in fuel consumption of 30-40% for long-haul flights, which includes the fuel used to perform the AAR. These improvements would be particularly noteworthy

for helicopters, which are generally much less fuel efficient compared to a fixed-wing aircraft and have a smaller operating range. As such, the overall objective of this work is to maximize the benefits of AAR technology by developing an AAR system for commercial applications, specifically non-military helicopter refuelling applications. This project is in collaboration with Wilderness North in Thunder Bay, Ontario.

1.2 Literature Review

Literature review is performed in this section for developments in AAR technology and the related modeling techniques. The focus will be on the control of flexible structures to simulate to the hose-drogue system.

1.2.1 Hose-Drogue System Modeling

Dynamic modeling for a flexible hose-drogue system is complex due to high nonlinearities experienced by the system during AAR procedures. For example, the hose catenary of a probe-drogue system largely depends not only on the speed of the aircraft, but also on turbulence from wind gusts and wing tip vortices, each of which varies with environmental conditions [12]. Further, the length of the flexible hose varies during AAR procedures, requiring the use of several distinct models to accurately capture system dynamics during hose deployment, full-trail, docking, and reeling operations. Several dynamic models are proposed in literature, which focus on specific operating conditions. A finite-segment-based numerical simulation was undertaken in [13] to approximate the dynamics of a probe-drogue assembly during hose deployment. Simulations showed the drogue exhibited significant nonlinear motions, particularly when passing through the aircraft wake. A computational fluid dynamics model was proposed to simulate the dynamic pressures exerted on the flexible hose-drogue surfaces towed behind a Su-33 geometric model at full-trail in [14]; simulations performed in this work indicated an unstable airflow field near the drogue existed for subsonic speeds. Both simulation results matched the experimental results obtained by NASA from an AAR flight test at its Dryden facility [15, 16]. During these tests it was found that an uncontrolled drogue towed behind an F/A-18A aircraft was unable to achieve a steady-state position relative to the tanker in the presence of turbulence.

Following hose deployment to full-trail length, engagement between the refueling probe and drogue is initiated by the receiver aircraft. This operation pushes the refueling drogue forward and introduces slack into the system, resulting in a sudden decrease in hose tension. Coupled with nonlinear aerodynamic forces, the sudden decrease in tension can result in a phenomenon known as "hose-whipping" wherein the alternating influences of tension and aerodynamic drag cause increasingly violent oscillatory motions in the refueling drogue. During hose-whipping oscillations, large transverse loads are applied to the probe, which can result in damage to the hose and drogue, or even cause catastrophic accidents. As a result, several methods of controlling the tension in the refueling hose were proposed. For example, simulations were performed in [17], which used an electric motor-driven hose reel in a tanker aircraft to control the tension on the hose during docking procedures. Some promising results were obtained in this study by controlling the angular velocity of the hose reel directly, but none of the proposed controllers would be capable of achieving robust control performance by manipulating the hose reel alone. A robust controller was proposed in [18] that utilized a relative-position strategy in combination with a permanent magnet synchronous hose reel motor to suppress hose-whipping vibrations during the docking procedure; but some discrepancies between simulated and experimental results remained. Accordingly, more advanced control strategies must be developed to accommodate the nonlinear characteristics exhibited by flexible structures.

1.2.2 System Control

Several control strategies have been proposed in literature to deal with the nonlinear dynamics of flexible structures. For simplicity, these strategies can be divided into two main categories: passive and active control. Passive control strategies are not explicitly based on a system model, but instead utilize energy dissipation devices to reduce vibrations without using external power [19]. Several types of dissipation devices are utilized, such as metallic dampers, friction dampers, viscoelastic dampers, viscous fluid dampers, tuned liquid dampers and tuned mass dampers [20]. Regardless of the type of device utilized, all dampers reduce system vibrations by dissipating kinetic energy into thermal energy. Passive control strategies can be used to provide cost-effective solutions for linear systems but are tuned to a specific load case. As a result, these controllers are less effective at suppressing vibrations for applications subject to dynamic loadings [21]. Common applications of passive control devices include seismic earthquake protection

4

systems for tall buildings [22-25], in which passive mass damping is applied to mitigate the potential seismic damage encountered during earthquakes in numerical simulations. Further, researches in [22-25] found that a passively controlled structure was subjected to a smaller magnitude of displacements in response to excitation compared to an uncontrolled structure. In [22] specifically, the placement of the damping devices was optimized for a tall multi-leveled structure for both a passive and an active control. A minor improvement was seen when an active controller was used instead of a passive controller, and both showed improved results compared to an uncontrolled structure.

As their name suggests, active control strategies operate actively to achieve vibration suppression by actively generated control forces to suppress system vibrations. The methodology of the generated control force varies depending on the active control strategies selected. As such, active control methods can be further divided into three categories: classical controllers, advanced controllers, and intelligent controllers as indicated in Figure 1.3.
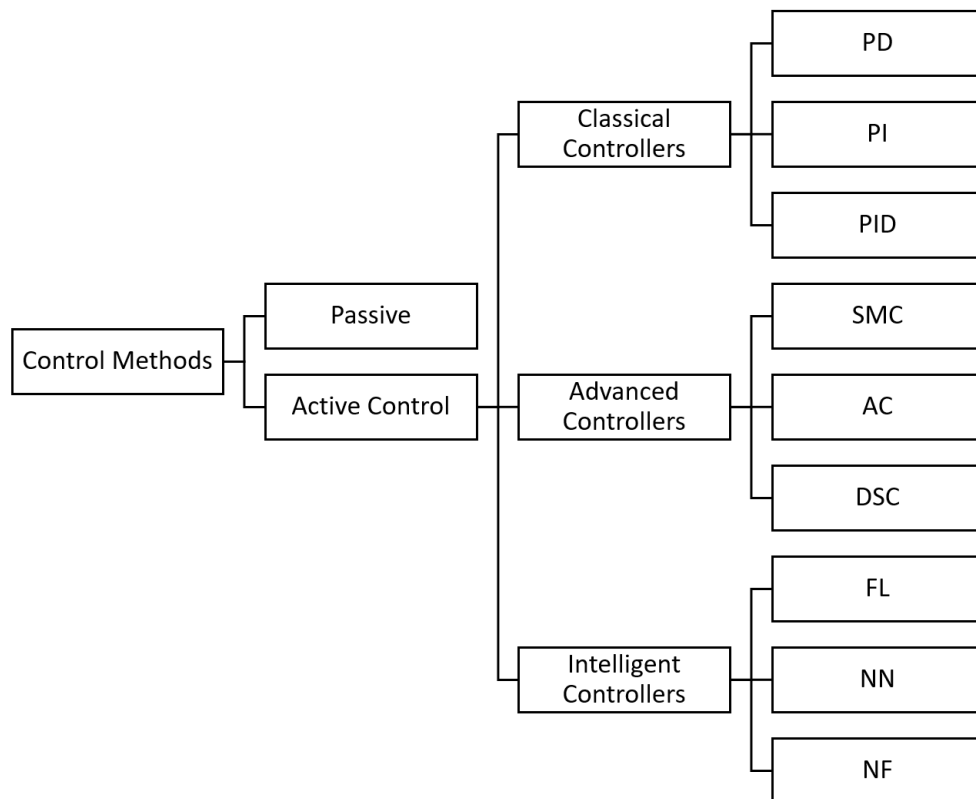
Figure 1.3: General control method classifications. PD: proportional-derivative, PI: proportional-integral, PID: proportional-integral-derivative, SMC: sliding-mode control, AC: adaptive control, DSC: dynamic surface control, FL: fuzzy logic, NN: neural network, and NF: neuro-fuzzy.

1.2.2.1 Classical Controllers

Classical controllers utilize a feedback control loop strategy to calculate the error between a setpoint and a measured process variable. A corrective control force is then applied based on proportional (P), integral (I), and derivative (D) control terms, respectively. Three-term or PID controllers are widely utilized in industrial applications due to their relatively robust control capabilities [26]. In [27], a PID controller was used to simulate the control of a three degrees of freedom (3-DOF) manipulator mounted to a flexible base mobile robot. Improvements to controller function in terms of overshoot and settling time were noted when additional gain optimization techniques were employed. The speed control of a direct current motor was simulated in [28] using several variations of a PID controller in combination with an adaptive neuro-fuzzy inference system (ANFIS) that was used to estimate nonlinear motor characteristics. Simulations showed that PD controllers outperformed PI controllers in terms of overshoot and settling time, however PID controllers exhibited even better performance characteristics, which are needed for robust control.

In general, the P term can account for the error between the setpoint and process variable to generate a control signal. The I term accounts for past errors between the setpoint and process variable and integrates the errors over time to generate a control signal. The D term is sometimes referred to as anticipatory control, which can be used to calculate future errors based on the rate of change between the setpoint and process variable in order to generate a control signal. The classical controller utilized is based on which control terms have been selected, but not all control terms need to be utilized to achieve the desired control operation. While three-term PID controllers are capable of delivering more robust control, any combination of control terms can be utilized to develop a controller. For example, it was found in [29] that a PD controller was sufficient for controlling the first six vibrational modes in a 3-DOF flexible manipulator. While the inclusion of the I term may allow for additional controller improvements, the magnitude of those improvements may not justify the effort required for their inclusion and optimization.

The main difficulty in the utilization of a classical controller is the determination of the control gain for each control term. Each term utilizing fixed control gains can be difficult to optimize to achieve desired performance, particularly in noisy plant environments. Several heuristic or nature-inspired methods have been utilized to optimize control gains so as to make

them easy to implement in applications without the determination of complex equations of motion. In [30], for example, the heuristic Ziegler-Nichols (ZN) tuning technique was employed to optimize the control gains of a PI controller for the control of a flexible beam; a fuzzy-tuned PID controller was also developed in this work, which could achieve better results in terms of solution convergence and vibration suppression. However, as the two separate controllers were utilizing two separate training algorithms, it was difficult to discern the feasibility of a heuristic optimization algorithm. The ZN tuning technique was also used to optimize the control gains of a PID controller for the control of a simulated double-link flexible robotic manipulator in [31] and controller parameters were optimized through the artificial bee colony and particle swarm optimization (PSO) algorithms; it was found that a PID controller with control gains optimized through the PSO algorithm was capable of achieving improved results compared to the ZN algorithm. In addition, several hybrid PID controllers were proposed in [32-36] that utilized fuzzy logic (FL) to approximate and self-tune controller gains for the control of flexible structures.

In industrial applications, more traditional optimization techniques are typically employed to optimize controller gains. One of the commonly utilized methodologies is the linear-quadratic-regulator (LQR) algorithm, which can be used to minimize the cost function of a dynamic system based on weighting factors supplied by a human expert. In [37] an LQR-based controller was proposed to suppress the vibration of a flexible boom in aerial refueling, and the stability of the proposed controller was verified using Lyapunov theory. This controller demonstrated good nonlinear approximation capabilities. This was also observed in [38] , which combined an energy storage system and a synchronous generator for frequency control, utilizing an extended LQR technique with an additional term to account for disturbance suppression. It was also found that the developed controller was superior to conventional PID and fuzzy control strategies in robust control.

1.2.2.2 Advanced Controllers

More advanced control techniques have been suggested in literature to address the issue of nonlinear system dynamics. Among these techniques, sliding mode control (SMC) is widely utilized due to its simplicity and resistance to changing system dynamics [39]. In SMC, the control signal depends on the system's current position in state space, and is used to drive a system to a desired position (i.e., the sliding surface). Instead of applying two oppositional control forces

across the sliding surface, SMC utilizes a discontinuous control signal for manipulation along the sliding surface. SMC can also be used for vibration suppression in flexible structures [40-44], utilizing a resistance to nonlinear system characteristics using the sliding mode methodology. Although these works demonstrated the control stability according to the Lyapunov theory, these controllers were subject to the chattering phenomenon to some degree. Chattering occurs when the control signal oscillates in a narrow region across the sliding surface, which is one of the main obstacles in using a SMC technique. There is the potential that SMC control actions in response to nonlinearities can induce additional vibrations into the solution space [43]. Methods were proposed in [40, 41] to reduce the prevalence of chattering at the cost of solution convergence accuracy. Generally, the available chattering mitigation techniques revolve around boundary layers, which could widen the sliding surface at the cost of control accuracy.

In adaptive control, control laws are adapted to accommodate changing conditions in the plant to ensure consistent closed-loop characteristics [45]. For example, the control law governing the flight of an aircraft would need to update in order to accommodate the consumption of fuel used during a flight, as the mass of the system decreases. As a result, the required control laws for systems subject to significant nonlinearities would be extremely complex or an "explosion of complexity" [46, 47]. This phenomenon can be reduced by limiting, or saturating, the range of input states for the controllers but at the cost of limiting the controllers' functionality in real-world applications. Two adaptive control methods are proposed in [48] for uncertain stochastic nonlinear systems. By using input constraints bounded by Lyapunov functions, the developed controller can properly approximate nonlinear trajectories. Further extensions to advanced controllers have been suggested, such as dynamic surface control (DSC), which utilize a series of first-order low pass filters in combination with a multiple sliding surface controller [49]. The proposed DSC in [50] was to govern a mobile wheeled inverted pendulum, while the DSC in [51] was to control an underactuated autonomous surface vehicle; both DSC methods could provide more robust control performance than conventional LQR controllers. However, in both cases, the model uncertainties and external disturbances were assumed to be bounded, which would limit the range of controller outputs.

1.2.2.3 Intelligent Controllers

In the last decade, many intelligent controllers have been proposed for nonlinear system control. FL uses easy-to-understand If-Then linguistic rules to model imprecise information; it also can facilitate knowledge implementation for human operators to incorporate their expertise into the design and improvement of the controller [52]. Compared to classical and advanced controllers, FL uses fuzzy If-Then rules to approximate uncertain nonlinear systems, or even imprecisely unknown system characteristics. For example, fuzzy backstepping control was used in [53] to determine the unknown nonlinear terms in a nonlinear strict-feedback system; the resulting controller was able to converge to the solution in a small area around the origin. In [54] FL control was used in combination with disturbance observers to accommodate unknown external disturbances to the inputs on a robotic exoskeleton's actuators; the resulting fuzzy control did not need the built-in torque sensing units. Several FL controllers have also been used in vibration suppression for flexible structures [55-57]. For example, a FL controller was used to control a tall building subjected to wind perturbations [58]; this study also found that the FL control performed better than classical linear-quadratic-Gaussian control for vibration suppression in flexible structures.

However, it is difficult for designers to determine optimal fuzzy system parameters by trial-and-error, since requisite expertise needs to be translated into the fuzzy rule form. FL systems themselves lack the learning capability required to adapt to changing system dynamics [52, 59]. Neural networks (NN), or artificial neural networks, are another type of popular intelligent tool that is used frequently in applications with changing system dynamics. NNs have two main network topologies: feedforward and recurrent architectures. Feedforward NNs utilize unidirectional links to generate an output from propagated inputs, whereas recurrent NNs also have some feedback links that allow nodal outputs to move backward within the NN structure as historical information. While more complicated, the recurrent NN topology has some distinct advantages, specifically in terms of access to historical data to improve reasoning accuracy.

NNs have been utilized in the control of flexible structures [60-63]. For example, in [64], a NN was used to achieve vibration suppression and accommodate for dynamic uncertainties of a tall flexible eccentrically loaded structure; it was also found that further control improvements were achieved, in terms of settling time and overshoot, through the use of output constraint. Similar

methodology was employed in [65], where a NN was used to address the issue of unknown dynamics in the control of a flexible structure; it was also shown that the NN controller performed better than a classical PD controller in vibration suppression This was mainly due to the unique learning capability of NNs to update controller parameters during the control sequence with changing system dynamics.

Training operations for NNs are performed by propagating training data pairs to update the neuron link weights, improving the mapping between the input space and the output space. In applications with a target output, supervised learning can be performed to allow a NN to approximate any continuous function. In applications without a specific target, weight updating procedures can still be employed to derive conclusions from large and unstructured datasets. The main drawback of a NN is related to its black-box processing; the resulting NN reasoning is opaque to users and difficult to interpret for knowledge processing.

In order to combine the merits of FL and NNs while tacking their respective limitations, an integrated solution of FL and NNs, or neuro-fuzzy (NF) system, has been used in engineering applications. A NF controller could be a more promising solution for approximating the nonlinear motions exhibited by a flexible structure subjected to changing system dynamics. Recently, several applications have utilized a NF controller for the control of a flexible structure [66-69]. A novel ANFIS-based control method was proposed in [70] for the control of a flexible-joint robot arm with resistance to changing dynamic conditions. An ANFIS-LQR controller was used in [71] to control an inverted rotary pendulum; the ANFIS was trained using data generated by the LQR controller, which displayed better resistance to dynamic conditions and enhanced system convergence to a steady state solution.

The performance of NF controllers can be improved by applying appropriate training algorithms. Generally, a hybrid strategy is used to train linear and nonlinear NF parameters, respectively. One of the most commonly utilized methods is the combination of least-squares estimator (LSE) and gradient descent (GD), to optimize the linear and nonlinear parameters respectively [59]. However, all gradient and derivative-based methods are sensitive to initial conditions and are prone to trapping in local minima [52]. Genetic algorithms are population-based meta-heuristic operators that perform a systematic random search; as such they are generally considered to be global search algorithms and can be applied to both continuous and discontinuous

functions, which could be used for NF system optimization [72-75]. Although these algorithms could have better performance for system identification at lower resonant modes, their main drawback is computationally expensive, which make them difficult to implement in real-time control applications. As such, there is a need for a more computationally efficient heuristic-inspired optimization technique that can be utilized for the optimization of NF parameters.

1.3 Objective of Research

The objective of this research is to develop a new AAR system for commercial applications, specifically for helicopter refuelling. In collaboration with Wilderness North in Thunder Bay, the fuel tanker will be a modified AT-802 called the FuelBoss. The first objective is to make a preliminary design of the AAR system.

The second objective is to suppress hose-drogue vibration in the AAR system. Since no real commercial application of AAR exists, a flexible structure is used to simulate the dynamic conditions of the hose-drogue system. An adaptive NF controller is developed for active vibration control of a flexible structure. The developed controller should be computationally efficient and easy to implement at a command-line level for high latency applications using the MATLAB platform. In order to suppress vibrations induced by control actions, an output suppression technique is proposed in order to adapt to changing system dynamics. A new recurrent learning algorithm is suggested for the optimization of non-linear NF parameters. The proposed algorithm utilizes a heuristic search strategy to improve convergence.

1.4 Thesis Organization

Each chapter in this work focuses on a specific topic of discussion. The remaining chapters in this work are organized as follows:

In Chapter 2, the theory related to AAR methodology is discussed. Characteristics of a representative system are identified and utilized in the formulation of appropriate modeling techniques.

Chapter 3 discusses the modeling and control of the flexible beam structure utilized in experimental procedures. The equations of motion are derived, and a state-space model is

developed for identification and control. Chapter 3 also discusses the design and implementation of an adaptive NF control system.

Chapter 4 describes the proposed bisection particle swarm optimization (BPSO) algorithm for the training of the nonlinear NF controller parameters. An output suppression technique is suggested to limit control action of the NF controller to reduce the prevalence of vibrations induced from control actions.

The effectiveness of the developed adaptive NF controller and the BPSO training algorithm is verified experimentally in Chapter 5. The controller's robustness to dynamics variation is tested by placing additional mass blocks at different locations on the flexible beam.

The concluding remarks and future works are outlined in Chapter 6.

Chapter 2
Modeling of an Aerial Refueling System

2.1 Overview

For aircrafts with a limited range, aerial refueling can be used to significantly extend the effective range by performing refueling operations mid-flight. Figure 2.1 illustrates the concept of the probe-drogue refueling system. As discussed in Chapter 1, probe-drogue refueling is performed by deploying a length of hose coupled to a drogue behind a tanker aircraft. The drogue is typically comprised of a rigid metal internal structure with a fabric canopy that is used to generate drag. On the receiver aircraft, a probe is installed which protrudes from the front surface that is piloted into the deployed drogue. After contact is achieved, the probe and drogue are mechanically coupled, and fuel transfer is initiated from the tanker to the receiver aircraft. After the desired amount of fuel is supplied, the hose is depressurized, the probe and drogue are decoupled, and the hose and drogue are retracted back into the tanker aircraft [76]. This agreement details the protocol for the specific flight maneuvers required for successful aerial refueling operations, as well as the general protocol for the interface between refueling components.

This work focuses on refuelling helicopters from the FuelBoss aircraft, and the concept is illustrated in Figure 2.1. This concept is based on a probe-drogue refueling system, which utilizes the flexibility of the refueling hose to maneuver around helicopters rotors. As the refueling hose is deployed from the FuelBoss, the flexibility of the refueling hose increases. However, an increased flexibility also introduces additional degrees of freedom in the form of torsional and elastic deformations [78]. Thus, the flexible refueling hose represents a classical underactuated system, making traditional control methods ineffective. Further, the mass of the hose changes during the refueling operations since the hose is purged of fuel before being retracted back into the FuelBoss. A reduction in system weight can introduce flexible modes, which result in additional vibrations in the steady state solution space [79, 80]. In system control practice these vibrations could degrade control performance with an increased convergence time and reduce the precision attainable by the controller, or even lead to control instability. Correspondingly, a new control strategy will be developed to accommodate for the introduced nonlinearities to the refueling hose during probe-drogue AAR.

Figure 2.1: Concept of plane-to-helicopter aerial refueling with a probe-drogue system [77].

2.2 System Components

There are two configurations of probe-drogue refueling systems that can be utilized with tanker aircrafts: a wing-mounted refueling pod and fuselage refueling systems. Both types utilize the same main components to accomplish AAR: a probe, a drogue, a hose drum unit, and a fuel pump. Wing pods are connected to the underside of an aircraft wing by means of a support pylon, as such the fairing of the pod and pylon are tailored to the specific aerodynamic requirements of the aircraft. Figure 2.2(a) shows an example of the wind pod configuration, including typical components and their placement. The main components of the refueling system are located within the refueling pod and the associated connections, including wiring and pipework, and are routed through the interior of the pylon. In order to maintain a balanced aerodynamic load, wing refueling pods are installed on each wing of an aircraft when utilized.

Fuselage refueling systems operate with a similar methodology, but all related components are housed internally within the fuselage of the tanker aircraft. This allows for a longer hose to be utilized and allows for the refueling of larger receiver aircraft with larger safe separation considerations [81]. An example of the fuselage refueling system configuration is shown in Figure 2.2(b).
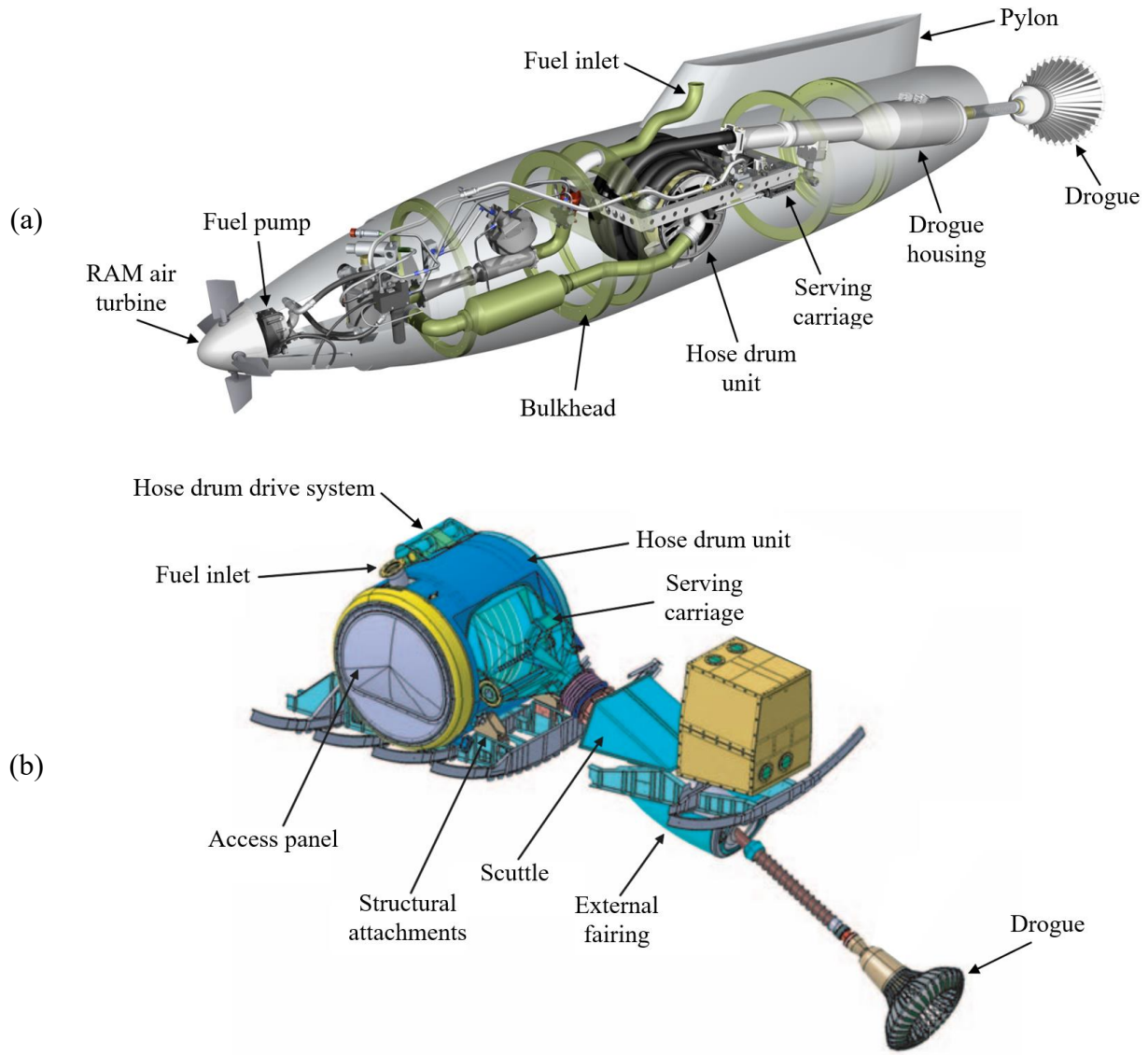
Figure 2.2: Probe-drogue configurations: (a) wing-mounted refueling pod [82], (b) fuselage refueling unit [76].

2.2.1 Probe

The fuel reservoir of the receiver aircraft receives fuel during AAR operations through mechanical coupling with a refueling probe. Probes are installed to the front surface of the receiver aircraft, and are either fixed, telescopic, or articulated. Fixed probes are permanent protrusions from the front surface, while telescopic probes have the capability to retract into the body of the receiver aircraft outside of AAR operations. Articulated probes are typically a combination of fixed and telescopic probes, which allow for a small degree of manipulation of the refueling probe. An example of a telescoping and articulated refueling probe are illustrated in Figure 2.3(a) and Figure 2.3(b), respectively. To prevent damage to the receiver aircraft, refueling probes are

purposefully designed with a weak link, regardless of the type utilized. This can prevent the transfer of excessive loads to the receiver aircraft but prevents future AAR procedures from being performed until the probe is repaired. Probe-drogue interface characteristics, such as probe positioning relative to receiver aircraft fuselage and operating envelopes, are outlined in NATO standard agreement (STANAG 3447) [84].

(a)

(b)
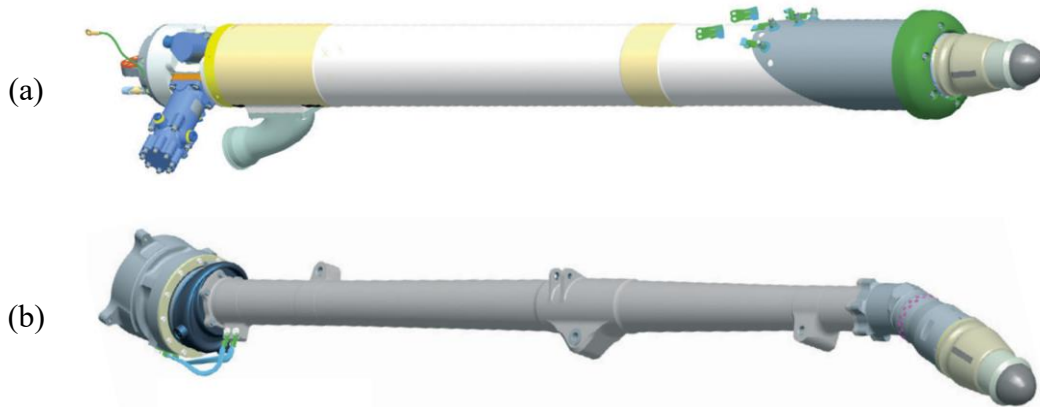
Figure 2.3: Aerial refueling probes: (a) telescoping probe [83], (b) articulated probe [83].

2.2.2 Drogue

Coupled to the end of the flexible refueling hose, a drogue is utilized to generate aerodynamic drag during the AAR procedure. Typical drogues are constructed with a collapsible, circumferential array of triangular struts, composed of either metal or polymer, and a fabric canopy, as illustrated in Figure 2.4.
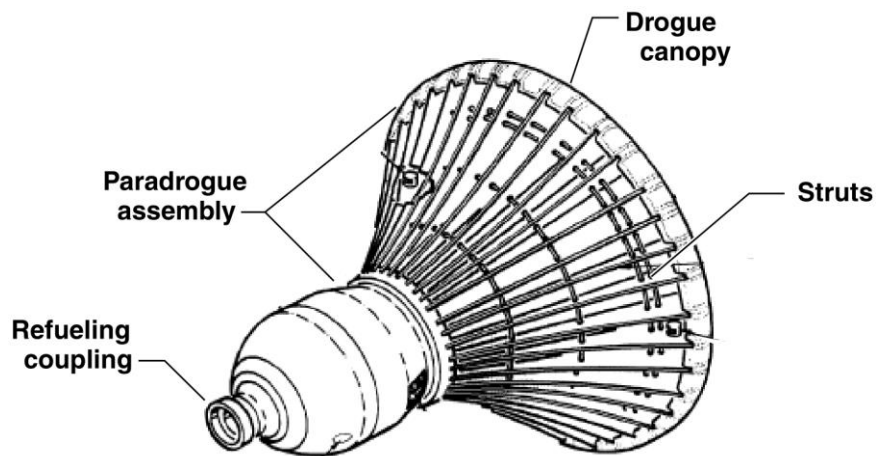
Figure 2.4: Diagram of an aerial refueling drogue [16].

Two different types of drogues are utilized in AAR operations: fixed and variable drag drogues. Fixed drogues utilize fixed geometry and are used for AAR operations with specific operating parameters. Variable drag drogues are designed such that the drogue area decreases with speed and can be utilized for a wider range of operating parameters. Typical AAR methodology solely uses the drag generated from a drogue to deploy the hose and drogue to the full-trail position. For helicopter refueling applications, only a low-speed drogue of a larger diameter is capable of providing the desired flight characteristics for aerial refueling [81].

2.2.3 Hose Drum Unit

Depending on the AAR methodology utilized, the hose drum unit is housed within a refueling pod or the fuselage of the tanker aircraft. The entire length of refueling hose is wound around a spool, as illustrated in Figure 2.5(a). The spooling and unspooling operations are performed automatically based on a hydraulic or electronic drive system. The most common hose drum units in aerial refueling applications use hydraulic drive systems, but recent applications see more frequent utilization of electronic drive systems [76]. Specialized serving carriage assemblies, such as the one shown in Figure 2.5(b), are typically utilized to orient the hose during spooling and unspooling operations, so that variations in layer depth and horizontal position can be accommodated dynamically [76].

(a)   (b)
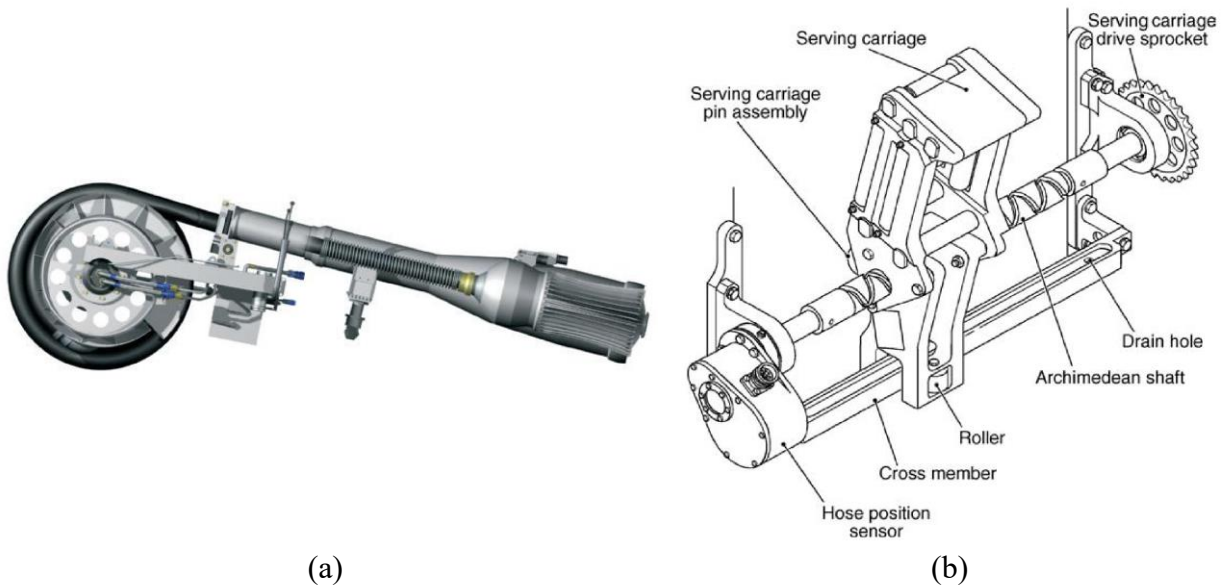
Figure 2.5: Hose drum unit: (a) coupled to a retracted aerial refueling drogue [85], (b) serving carriage [76].

Hose drum units utilize an electronic brake to prevent unspooling outside of AAR operations and to prevent additional unspooling after the full-trail length has been achieved. After mechanical coupling between the probe and drogue, the hose drum unit begins spooling operations to take-up the resulting slack. After retracting a set distance, the hose is pressurized, and fuel transfer is initiated. MA-2/3/4 couplings are commonly utilized in AAR procedures and are designed to deliver fuel at 50 ± 5 psig [86]. When the refueling operation is completed the receiver aircraft slows, and the hose is unspooled back to the full-trail position. Then, the hose is depressurized, and the receiver aircraft disconnects by pulling away from the refueling drogue.

2.2.4 Additional Components

Several additional components are utilized in the AAR system, depending on the specific scope and requirements of the application. Several fuel system components are necessary for system function, such as surge suppressors, fuel filters, pressure and temperature sensors, and fuel pumps [87]. Figure 2.6 illustrates the fuel components of a typical aerial refueling system and its layout. Typical application uses hydraulic or electric centrifugal-type fuel pumps for fuel delivery. Some specialized fuel pumps in AAR systems utilize a ram-air turbine with variable pitch control to drive fuel delivery. Furthermore, most commercial AAR systems fully rely on the aircraft power for system function.
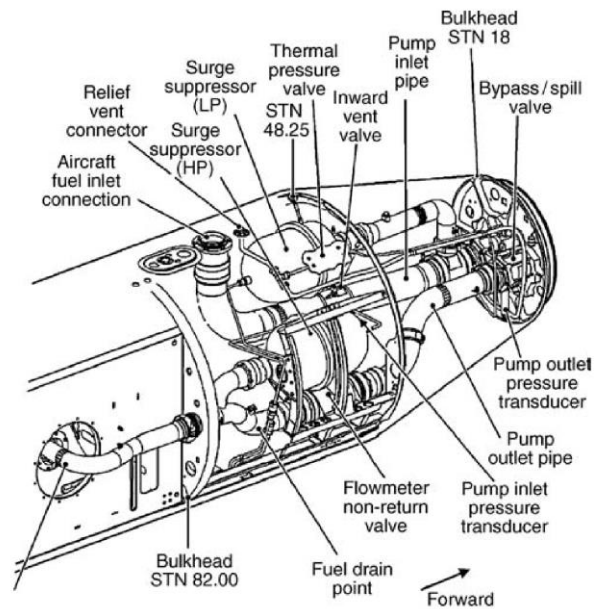
Figure 2.6: Fuel system layout of an AAR wing pod [76].

2.2.5 FuelBoss Aircraft

The development of a new AAR system for commercial applications is performed collaboratively with Wilderness North, an industry partner based out of Thunder Bay, Ontario. The tanker aircraft selected for the application is Wilderness North's FuelBoss, shown in Figure 2.7, a modified AT-802 with a removable auxiliary fuel tank mounted to the underbelly of the airplane. This fuel tank has a maximum capacity of 4000 L and allows the aircraft to perform large fuel deliveries to remote communities in Northwestern Ontario. The developed AAR system will interface with receiver aircrafts and deliver fuel from the FuelBoss' auxiliary fuel tank.

Figure 2.7: Wilderness North's FuelBoss aircraft with an auxiliary fuel tank [3].

2.3 Drogue Control

The success of an AAR operations depends primarily on a system's ability to suppress nonlinear oscillations when sail away or hose waves occurs. Sail away occurs when the receiver aircraft pushes the drogue forward, either from its bow wave or physical probe contact, before mechanical coupling is achieved. As a result, the drogue moves away from the receiver aircraft, and the AAR operation is aborted. Hose wave oscillations can occur as a result of a high-speed contact, either from a receiver aircraft's bow wave, physical probe contact, or a suboptimal approach direction; it will introduce slack into the flexible hose by suddenly decreasing hose tension. The slack is subjected to the alternating influences of tension and aerodynamic drag, which oscillates up and down the length of the hose, eventually degrading into increasingly violent oscillatory motions.

A general rule-of-thumb is that drogue oscillations exceeding one-half the diameter of the drogue are too large for AAR operations [76, 88]. More sophisticated hose drum units are capable of dynamically adjusting the tension in the refueling hose to achieve some degree of oscillation suppression but are not capable of eliminating nonlinear oscillations entirely [17, 18] As such, several active control methods have been proposed in literature to suppress the nonlinear oscillations of an aerial refueling drogue. For example, patent [89] proposes the use of four directional thrusters to achieve control; patent [90] suggests control through a gyroscopically stable rotating mass; and patent [91] uses a rotatable control unit to provide tangential control forces. Unfortunately, research and development in drogue control are in their infancy, and very limited resources of real-world application are available for review.

However, one method of active drogue control was demonstrated in [92], in which active drogue control was achieved through the manipulation of four servo-actuated aerodynamic control surfaces. The control surfaces were circumferentially arranged around a refueling drogue and actuated to apply control forces based on sensor measurements to suppress drogue oscillations. In wind tunnel tests, a 1/3 scale hose and drogue prototype achieved a 90% reduction in drogue motion from external disturbances. However, it was noted that a discontinuity between simulations and experimental results lead the authors to adjust the controller gains to favor experimental results, highlighting the inaccuracy of the developed control law. Furthermore, experimental results indicated controller degradation at some dynamic pressures, suggesting that the proposed controller may not be appropriate for high frequency oscillations. More importantly, the experimental results were limited in scope since the setup utilized a rigid bar in place of a flexible refueling hose. The flexible nature of a refueling hose is a major contributing factor to the nonlinear oscillations experienced by an aerial refueling drogue during AAR operations. As such, one of the objectives of this work is to propose a new active control technique for the active vibration suppression of an aerial refuelling drogue.

In literature, active mass damping has been utilized in several applications to control the vibration of flexible structures [64, 71, 93, 94]. However, to the best of the author's knowledge, this methodology has never been applied to achieve vibration suppression of an aerial refueling drogue during AAR operations. The system illustrated in Figure 2.8 is proposed in order to apply an appropriate control force. In this system sliding point masses are appositionally located on the

exterior drogue, which will actuate in response to measured drogue displacements to suppress nonlinear oscillations.
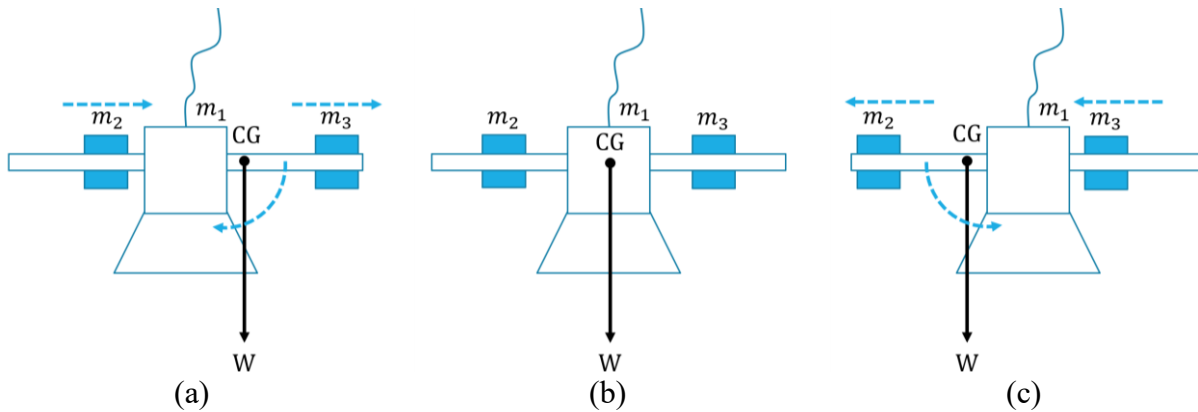
Figure 2.8: Sliding mass damping technique for drogue control: (a) clockwise rotation mode, (b) neutral mode, (c) counter-clockwise rotation mode.

Because there are no proper systems available to support this research, a flexible structure is used to undertake the proposed research work and develop a new controller to suppress the vibrations. The experimental setup utilizes rotationally actuated active mass damping instead of the linear methodology illustrated in Figure 2.8. As a result, this work demonstrates the feasibility of using active mass damping for the vibration suppression of flexible structures. It should be stated that this methodology may not be directly compatible with the AAR procedure, since the rotating mass may collide with the refueling probe. As such, further works need to utilize a more appropriate workstation in the future.

2.4 System Modeling

To assist in the development of an AAR system for the FuelBoss, several models are developed in this section, including a 3D model of the FuelBoss airplane and its internal structure. It also includes a preliminary design of a refueling unit, the development of specialized design tools, and the preliminary modeling and control of a representative flexible hose system.

2.4.1 Aircraft Modeling

A 1:1 3D model of the FuelBoss is developed to assist the preliminary design process, as shown in Figure 2.9. It allows the dimensions of refueling components to be more accurately

approximated. This is particularly useful in the determination of an effective means of drogue deployment, allowing for minimal interference with exterior control surfaces, such as the rudder and elevators.

Figure 2.9: Aircraft modeling: (a) reference AT-802F [95]. (b) 3D model of FuelBoss with auxiliary fuel tank.

Additional modeling of the interior FuelBoss structure is performed to assist in the development of each component's effective envelope. Figure 2.10 shows a developed 3D model of the rear internal structure of the FuelBoss, since all components are to be housed internally within the rear of the aircraft fuselage. This allows dimensions of refueling components to be sized more appropriately during the iterative design process. This model can also assist in the determination of an internal component layout that is the most conducive for AAR operations on the FuelBoss platform.

Figure 2.11 shows the proposed layout model, which includes the hose drum unit, indexer shroud, hose guide, and drogue housing.

(a)

(b)

Figure 2.10: Fuselage modeling: (a) FuelBoss rear fuselage, (b) 3D model of the FuelBoss rear fuselage internal structure.

(a)   (b)
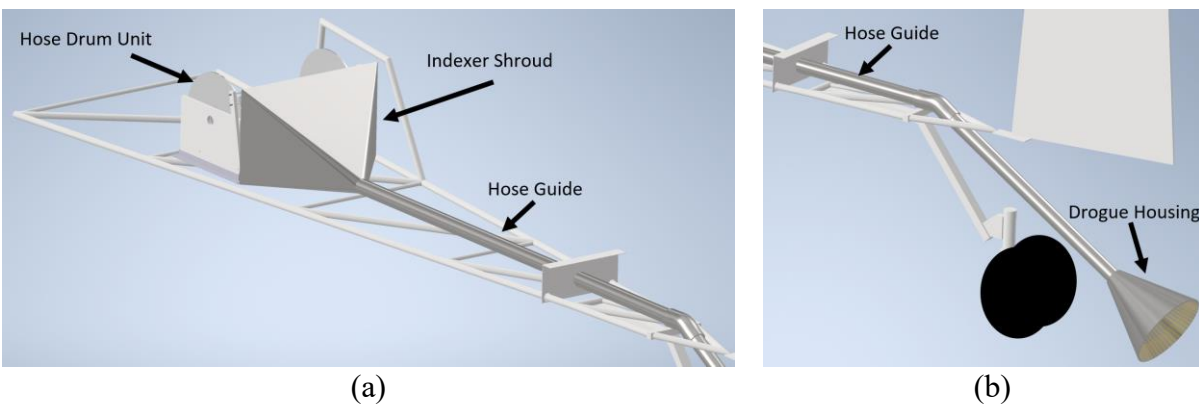
Figure 2.11: Potential installation location of preliminary AAR components: (a) components placed within the rear fuselage, (b) components exiting the rear fuselage behind the rear landing gear.

2.4.2 Component Modeling

Through the utilization of the 3D FuelBoss model, preliminary designs for the hose drum unit, indexer shroud, hose guide and drogue housing are developed. Each preliminary design is modified iteratively, based on criteria from the desired installation location and research team feedback. In the case of the hose drum unit, more specialized modeling techniques are required to ensure the correct length of refueling hose is compatible with the desired dimensions. Subsequently, an iterative design tool based on an experimental packing factor technique is developed as illustrated in Figure 2.12.
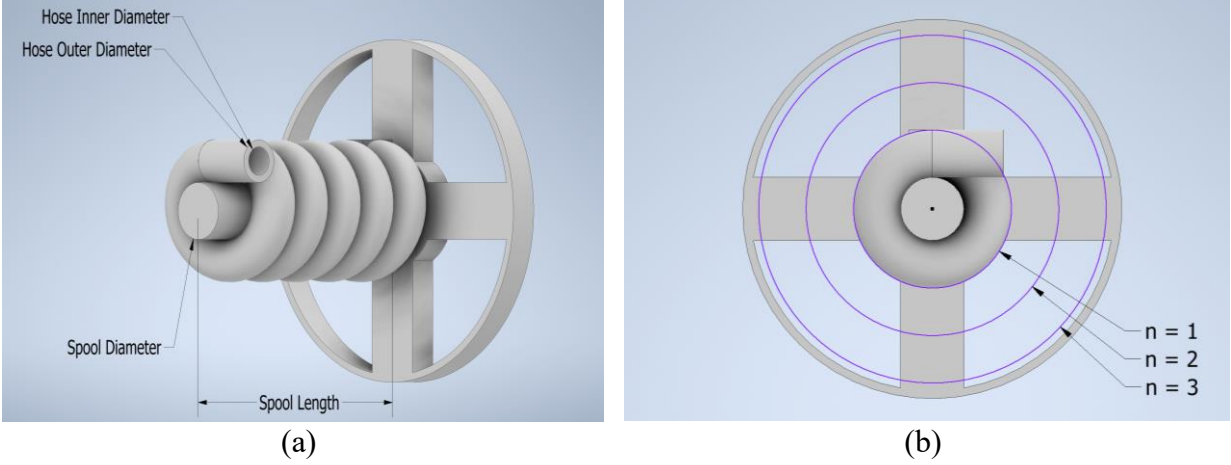
Figure 2.12: Model parameters for the hose drum unit design tool: (a) hose drum dimension parameters, (b) layer depth parameter.

Due to the inherent nature of the material, it can be reasonably expected that several gaps will exist when wrapping a flexible hose around a rigid spool. The magnitude of these gaps can be approximated by drawing several lengths of a representative hose tightly around a unit length of a spool. A packing factor-based relationship can then be established by simulation, based on the actual volume of the hose wrapped around the spool compared to the total volume of the layer. The total volume layer is determined by drawing a solid cylinder that touches the boundaries of the flexible hose, with the following packing factor relationship:

$$PF = \frac{\text{Actual Volume of Hose in Layer}}{\text{Total Volume of Layer}} \tag{2.1}$$

$$PF = \frac{\left(\frac{D_{h,o}}{2}\right)^2 \cdot L_h}{\left[\left(\frac{D_s}{2} + D_{h,o}\right)^2 - \left(\frac{D_s}{2}\right)^2\right] \cdot L_s} \tag{2.2}$$

where $D_{h,o}$ is the outer diameter of the hose, L_h is the length of the hose, D_s is the diameter of the spool, and L_s is the length of the spool.

This relationship can be adapted for additional layers of hose such that:

$$PF = \frac{\left(\frac{D_{h,o}}{2}\right)^2 \cdot L_h}{\sum_{n=1}^{k}\left[\left(\left(\frac{D_s}{2} + D_{h,o} + (n-1)D_{h,o}\right)^2 - \left(\frac{D_s}{2}\right)^2\right) \cdot L_s\right]} \tag{2.3}$$

where k is total number of hose layers.

By determining the packing factor, one can solve for the length of hose and determine if the selected hose parameters are compatible with the desired hose and drum unit dimensions. Consider the parameters outlined in Table 2.1, from Equation (2.3) L_h will be

$$L_h = 973.56\text{in} \tag{2.4}$$

Since the desired length of hose exceeds the calculated length of hose, it can be concluded that the hose drum unit dimensions are compatible. As the design tool generates component dimensions, additional calculations can be performed to estimate the component weight. From the above calculation, the estimated hose drum unit weight is 90.48 lbs without fuel (dry), which is 111.01 lbs with fuel.

Table 2.1: Hose-drum unit design tool parameters.

Symbol	Description	Value
$D_{h,i}$	Internal diameter of hose	1 in
$D_{h,o}$	External diameter of hose	1.5 in
D_s	Spool diameter	5 in
$L_{h,d}$	Length of hose (desired)	75 ft (900 in)
L_s	Length of spool	20 in
PF	Packing factor	0.6405
k	Number of layers of hose	3

2.4.3 Hose Simulations

To develop an approach for the control of the flexible hose, simulations are first performed to model a representative system with nonlinear oscillations. Figure 2.13 shows the developed preliminary model based on the double-pendulum system, which represents a classical underactuated system and has the following equations of motion:

$$(m_1 + m_2)\ell_1\ddot{\theta}_1 + m_2\ell_2\ddot{\theta}_2 \cos(\theta_2 - \theta_1) = m_2\ell_2\dot{\theta}_2^2 \sin(\theta_2 - \theta_1) - (m_1 + m_2)g \sin(\theta_1) \tag{2.5}$$

$$\ell_2\ddot{\theta}_2 + \ell_1\ddot{\theta}_1 \cos(\theta_2 - \theta_1) = -\ell_1\dot{\theta}_1^2 \sin(\theta_2 - \theta_1) - g \sin(\theta_2) \tag{2.6}$$

where:

$$\dot{\theta} = \omega = \frac{d\theta}{dt} \tag{2.7}$$

$$\ddot{\theta} = \alpha = \frac{d^2\theta}{dt^2} \tag{2.8}$$

Table 2.2: Parameters for modeling double-pendulum oscillations.

Symbol	Description	Value
θ_1	Link angle of link 1	$\pi/4$ (Initial position)
θ_2	Link angle of link 2	$\pi/2$ (Initial position)
ℓ_1	Length of link 1	25 m
ℓ_2	Length of link 2	5 m
m_1	Point mass 1	5 kg
m_2	Point mass 2	25 kg

The equations of motion in Equations (2.5) and (2.6) are then solved by using a fourth-order Runge-Kutta scheme, using the parameters listed in Table 2.2. As illustrated in Figure 2.14, simulations with an initial displacement can quickly result in nonlinear oscillation.
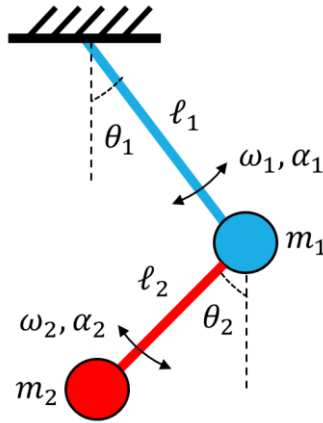
Figure 2.13: Double-pendulum system representing a flexible hose.

To assess the feasibility of the proposed active mass damping methodology, simulated proportional control actions are applied to the system. The angle of the second pendulum link (θ_2) is modified according to the position (θ_1) and velocity ($\dot{\theta}_1$) of the first pendulum link. Figure 2.15 displays the results of the controlled double-pendulum system. It is clear that active mass damping is capable of reducing the magnitude of nonlinear oscillations in an underactuated system. The simulated proportional controller uses unoptimized controller gains; although no immediate reduction in the magnitude of oscillations can be observed in Figure 2.15, the system eventually converges to a steady state solution.
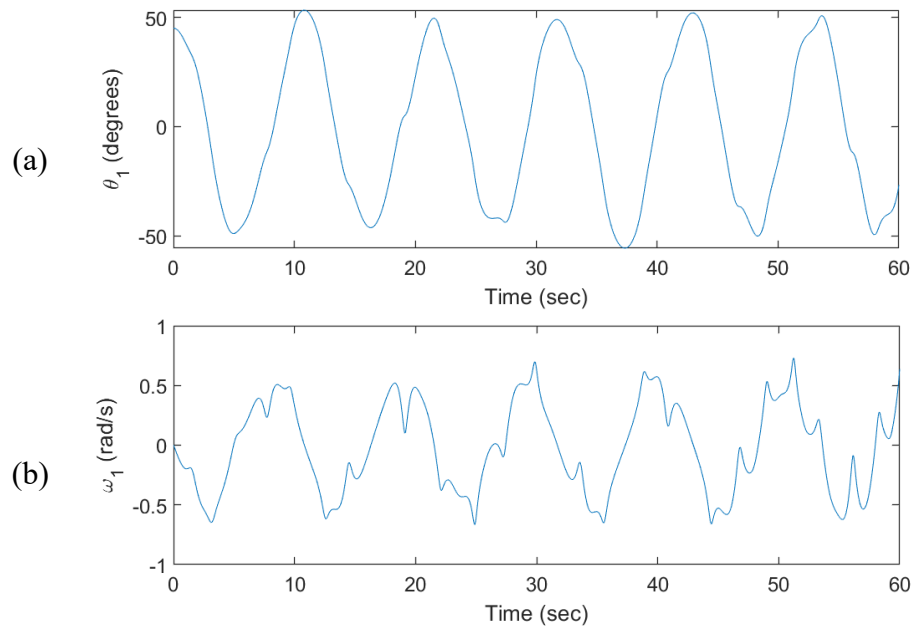
Figure 2.14: Simulation results of a double pendulum system with initial displacements: (a) angle of the upper link, (b) angular velocity of the upper link.
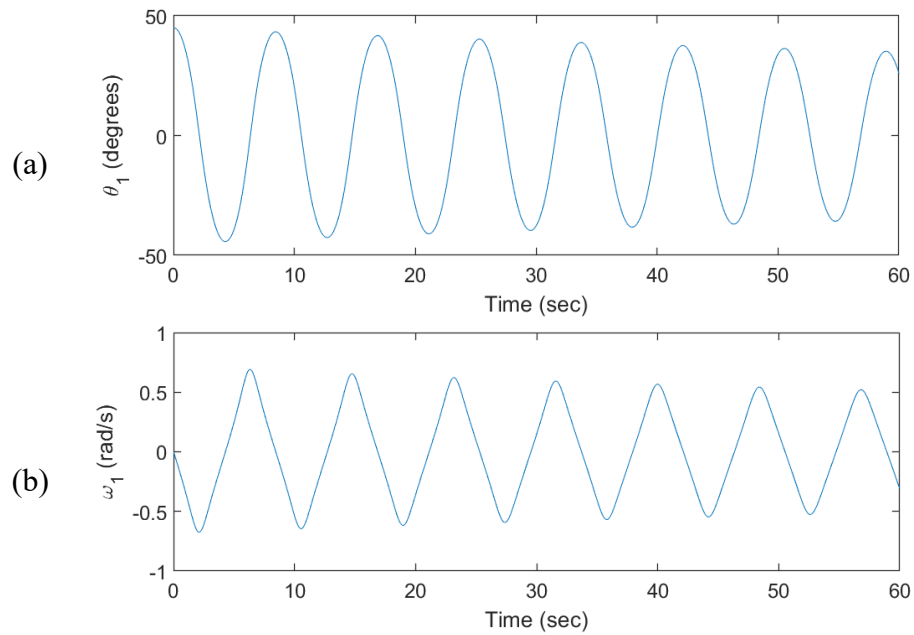
Figure 2.15: Simulation results of a double pendulum system with active mass damping and initial displacements: (a) angle of the upper link, (b) angular velocity of the upper link.

Chapter 3
System Modeling

3.1 Experimental Setup

In order to validate the performance of the proposed NF controller and BPSO training algorithm for the control of flexible structures, some tests are undertaken using the experimental setup as shown in Figure 3.1, which is adopted from the Quanser Smart Structure. The flexible beam is clamped at one end and free at the other. The DC drive motor is attached to the free end of the flexible beam, which drives a rigid rotary dual-bar linkage through a gear train with a total gearbox ratio of 70. An optical-shaft encoder with 4096 counts per revolution is used to measure the angular position of the rigid rotary bar in quadrature mode [96]. The deflection of the flexible beam is measured by a dual grid half bridge strain gauge secured to the bottom of the beam. This setup also features the ability to simulate variable dynamic loading conditions by placing additional mass blocks at different locations along the length of the flexible beam. All devices utilized in the experimental setup are powered with a dedicated power amplifier (UPM-24-05 from Quanser) [97], which is capable of supplying a maximum output voltage of 24 V at 5.0 A.
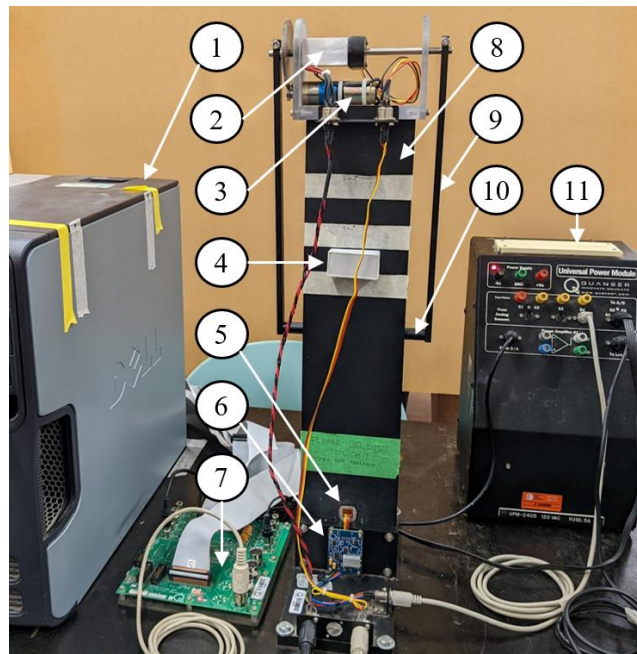
Figure 3.1: The experimental setup:(1)-computer with data acquisition card, (2)-encoder, (3)-motor, (4)-additional mass blocks, (5)-strain gauges, (6)-signal conditioning board, (7)-I/O terminal board, (8)-flexible beam, (9)-rigid bar, (10)-cross bar, (11)-power amplifier.

The analog deflection signal is measured through a signal conditioning board, which is calibrated such that a 1-inch deflection of the tip of the flexible beam corresponds to 1 V output signal. The deflection of the flexible beam and the angular position of the rigid bar are sent to a Q4 I/O terminal board as an analog and digital input, respectively. The terminal board interface with a data acquisition (DAQ) card, allowing the signals to be output to an adjacent dedicated PC. Using Quanser Hardware-in-the-Loop software development kit drivers [98], MATLAB programs can be written using command-line functions to implement controllers for use in experimental procedures. The DAQ card utilized allows for simultaneous sampling of both analog and digital signals [99].

3.2 Equations of Motion

The experimental setup consists of a motor structure with mass m_b, which is mounted to the top of a thin flexible beam. A rigid bar of length ℓ_p is connected to the motor and controls the angular position of mass m_p. A free-body diagram of the flexible structure can be found in Figure 3.2.
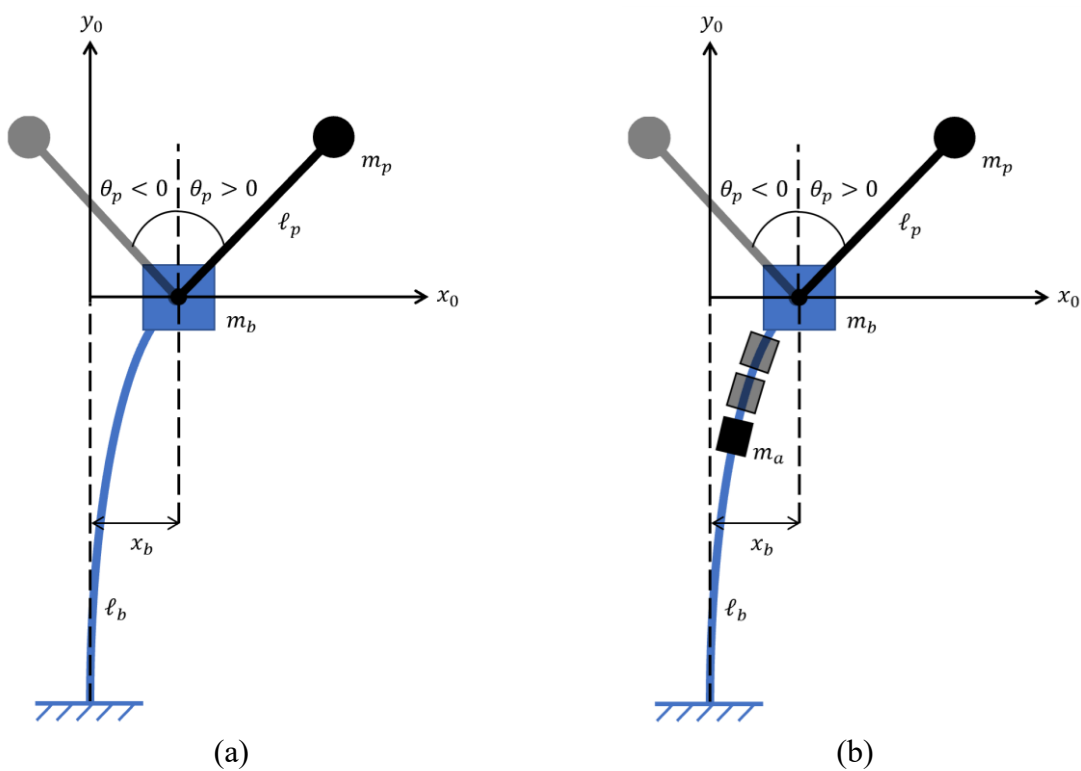
Figure 3.2: Free-body diagrams of the flexible structure: (a) without modification, (b) with dynamic loading in the form of additional mass blocks.

Using the Euler-Lagrange method, a set of nonlinear equations will be derived to describe the beam's motion in terms of the linear translation of the flexible beam and the angle of the rigid bar. Firstly, the flexible link is modeled as a mass-spring system as illustrated in Figure 3.3:
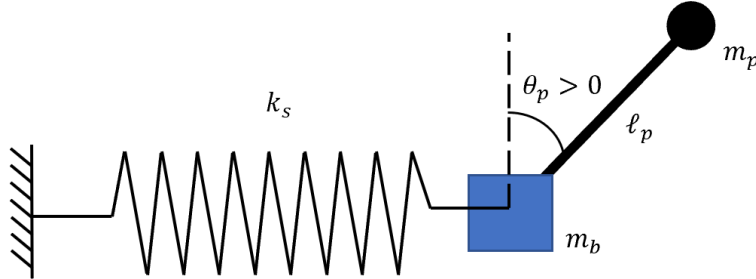
Figure 3.3: Simplified flexible link modeling.

where k_s is the spring constant of the massless spring representing the flexible beam, m_b is the mass of the motor structure, ℓ_p is the length of the rigid bar, m_p is the mass attached to the end of the rigid bar, and θ_p is the angle of the rigid bar. To simplify the development of the equations of motion, the rigid bars are assumed to be massless.

The potential energy of the spring can be expressed as:

$$P_1 = \frac{1}{2} k_s x_b^2 \tag{3.1}$$

where x_b is the linear displacement of the motor structure. The spring constant is determined using the following relationship:

$$\omega_n = \sqrt{\frac{k_s}{m_b + m_p}} \tag{3.2}$$

$$k_s = \omega_n^2 (m_b + m_p) \tag{3.3}$$

where ω_n is the natural frequency of the flexible beam used in experimental procedures. Detailed procedures outlining its determination can be found in Section 3.4.

The potential energy of the pendulum weight can be expressed as:

$$P_2 = m_p g (\cos \theta_p) \cdot \ell_p \tag{3.4}$$

Then total potential energy of the system is:

$$V = P_1 + P_2 \tag{3.5}$$

$$V = m_p g \left(\cos \theta_p \right) \ell_p + \frac{1}{2} k_s x_b^2 \tag{3.6}$$

Now, consider the kinetic energy from the translation of the motor structure:

$$K_1 = \frac{1}{2} m_b \dot{x}_b^2 \tag{3.7}$$

where $\dot{x}_b$ is the first derivative of the linear displacement of the motor structure with respect to time. Consider the kinetic energy from the rotation of the pendulum:

$$K_2 = \frac{1}{2} J_p \dot{\theta}_p^2 \tag{3.8}$$

where J_p is the moment of inertia of the motor and rotary arm, and $\dot{\theta}_p$ is the first derivative of the angle of the pendulum with respect to time. Consider the following relation relating linear and angular velocity:

$$v = \omega \cdot r \tag{3.9}$$

Equation (3.9) has the following form in this application:

$$v = \dot{\theta}_p \cdot \ell_p \tag{3.10}$$

Thus, the x- component of the linear velocity of pendulum arm will be:

$$v_{p,x} = \dot{\theta}_p \cos\left(\theta_p \right) \ell_p + \dot{x}_b \tag{3.11}$$

Similarly, the y- component of the linear velocity of the pendulum arm will be:

$$v_{p,y} = \dot{\theta}_p \sin\left(\theta_p \right) \ell_p \tag{3.12}$$

Taking the norm of the x- and y- velocity components:

$$v_{p,norm} = \sqrt{\left(\dot{\theta}_p \cos\left(\theta_p \right) \ell_p + \dot{x}_b \right)^2 + \left(\dot{\theta}_p \sin\left(\theta_p \right) \ell_p \right)^2} \tag{3.13}$$

Thus, the kinetic energy from the translation of the pendulum arm will be:

$$K_3 = \frac{1}{2} m_p v_{p,norm}^2 = \frac{1}{2} m_p \left(\left(\dot{\theta}_p \cos\left(\theta_p \right) \ell_p + \dot{x}_b \right)^2 + \left(\dot{\theta}_p \sin\left(\theta_p \right) \ell_p \right)^2 \right) \tag{3.14}$$

The total kinetic energy of the system is:

31

$$T = K_1 + K_2 + K_3 \tag{3.15}$$

$$T = \frac{1}{2}m_b\dot{x}_b^2 + \frac{1}{2}J_p\dot{\theta}_p^2 + \frac{1}{2}m_p\left(\left(\dot{\theta}_p\cos(\theta_p)\ell_p + \dot{x}_b\right)^2 + \left(\dot{\theta}_p\sin(\theta_p)\ell_p\right)^2\right) \tag{3.16}$$

The Euler-Lagrange equations have the following form:

$$\frac{\partial}{\partial t}\left(\frac{\partial L}{\partial \dot{x}_b}\right) - \left(\frac{\partial L}{\partial x_b}\right) = Q_1 \tag{3.17}$$

$$\frac{\partial}{\partial t}\left(\frac{\partial L}{\partial \dot{\theta}_p}\right) - \left(\frac{\partial L}{\partial \theta_p}\right) = Q_2 \tag{3.18}$$

where Q_1 and Q_2 are generalized forces, and L is the Lagrangian with the form:

$$L = T - V \tag{3.19}$$

where T is the kinetic energy of the system, V is the potential energy of the system. However:

$$\frac{\partial V}{\partial \dot{x}_b} = 0 \tag{3.20}$$

$$\frac{\partial V}{\partial \dot{\theta}_p} = 0 \tag{3.21}$$

Then:

$$\frac{\partial L}{\partial \dot{x}_b} = \frac{\partial T}{\partial \dot{x}_b} \tag{3.22}$$

$$\frac{\partial L}{\partial \dot{\theta}_p} = \frac{\partial T}{\partial \dot{\theta}_p} \tag{3.23}$$

which allows a simplified form of Equation (3.17) and (3.18) to be used:

$$\frac{\partial}{\partial t}\left(\frac{\partial T}{\partial \dot{x}_b}\right) - \left(\frac{\partial T}{\partial x_b}\right) + \left(\frac{\partial V}{\partial x_b}\right) = Q_1 \tag{3.24}$$

$$\frac{\partial}{\partial t}\left(\frac{\partial T}{\partial \dot{\theta}_p}\right) - \left(\frac{\partial T}{\partial \theta_p}\right) + \left(\frac{\partial V}{\partial \theta_p}\right) = Q_2 \tag{3.25}$$

The generalized forces applied to the system are:

$$Q_1 = B_b\dot{x}_b \tag{3.26}$$

$$Q_2 = \tau_m - B_p \dot{\theta}_p \tag{3.27}$$

where B_b is the flexible beam viscous friction torque coefficient, B_p is the pendulum viscous friction torque coefficient, and τ_m is the torque produced by the motor at the motor pinion.

For the motor utilized in the experimental setup, the torque produced will be

$$\tau_m = \frac{\eta_g K_g \eta_m k_t \left(V_m - K_g k_m \dot{\theta}_p \right)}{R_m} \tag{3.28}$$

$$\tau_m = \frac{\eta_g K_g \eta_m k_t V_m}{R_m} - \frac{\eta_g K_g^2 \eta_m k_t k_m \dot{\theta}_p}{R_m} \tag{3.29}$$

The related motor parameters are summarized in Table 3.1.

If viscous damping parameters B_b and B_p are neglected, the generalized forces applied to the system become:

$$Q_1 = 0 \tag{3.30}$$

$$Q_2 = \frac{\eta_g K_g \eta_m k_t}{R_m} V_m - \frac{\eta_g K_g^2 \eta_m k_t k_m}{R_m} \dot{\theta}_p \tag{3.31}$$

which results in the following equations of motion:

$$\left(m_b + m_p \right) \ddot{x}_b + m_p \ell_p \cos(\theta_p) \ddot{\theta}_p - m_p \ell_p \sin(\theta_p) \dot{\theta}_p^2 + k_s x_b = 0 \tag{3.32}$$

$$\left(J_p + m_p \ell_p^2 \right) \ddot{\theta}_p + m_p \cos(\theta_p) \ell_p \ddot{x}_b - m_p g \sin(\theta_p) \ell_p = \frac{\eta_g K_g \eta_m k_t}{R_m} V_m - \frac{\eta_g K_g^2 \eta_m k_t k_m}{R_m} \dot{\theta}_p \tag{3.33}$$

Detailed derivation of the equations of motion can be found in Appendix B.

Table 3.1: Motor parameters for the equations of motion [96].

Symbol	Description	Value
η_g	Gearbox efficiency	0.90±10%
K_g	Total gearbox ratio	70
η_m	Motor efficiency	0.69±5%
k_t	Motor torque constant	7.68E-03 N · m
V_m	Motor input voltage	Variable
k_m	Back-emf constant	7.68E-03 V/(rad/s)
R_m	Motor armature resistance	2.6 Ω

3.3 Preliminary Controller

A preliminary PD controller is to be developed to establish baseline vibration suppression in the flexible structure, and has the following form:

$$u = -k_{p,x}x_b - k_{p,\theta}\theta_p - k_{d,x}\dot{x}_b - k_{d,\theta}\dot{\theta}_p \tag{3.34}$$

where u is a generalized control signal; $k_{p,x}$ and $k_{p,\theta}$ represent the P-term gains for the deflection and angular position, respectively; and $k_{d,x}$ and $k_{d,\theta}$ represent the D-term gains for the deflection velocity and angular velocity respectively. This subsection outlines the development of an LQR-based (Linear-Quadratic-Regulator) state feedback control system for the generation of preliminary neuro-fuzzy (NF) training data.

We begin by considering the previously derived equations of motion Equation (3.32) and Equation (3.33). First, the derived equations of motion are linearized around the quiescent point of operation for small amplitude oscillations, where $\theta_0 = 0$. This allows the following simplifications to be used:

$$\sin\theta_0 \approx \theta \tag{3.35}$$

$$\cos\theta_0 \approx 1 \tag{3.36}$$

$$\dot{\theta}_0^{\,2} = 0 \tag{3.37}$$

Thus, the resulting equations of motion become:

$$(m_b + m_p)\ddot{x}_b + m_p\ell_p\ddot{\theta}_p + k_s x_b = 0 \tag{3.38}$$

$$(J_p + m_p\ell_p^2)\ddot{\theta}_p + m_p\ell_p\ddot{x}_b - m_p g\ell_p\theta_p = \frac{\eta_g K_g \eta_m k_t}{R_m}V_m - \frac{\eta_g K_g^2 \eta_m k_t k_m}{R_m}\dot{\theta}_p \tag{3.39}$$

Consider the following state space variables:

$$\mathbf{q} = \begin{bmatrix} q_1 \\ q_2 \\ q_3 \\ q_4 \end{bmatrix} = \begin{bmatrix} x_b \\ \theta_p \\ \dot{x}_b \\ \dot{\theta}_p \end{bmatrix} \tag{3.40}$$

With linear state-space equations in the form:

$$\dot{\mathbf{q}} = \mathbf{A}\mathbf{q} + \mathbf{B}u \tag{3.41}$$

34

$$\boldsymbol{r} = \boldsymbol{C}\boldsymbol{q} + \boldsymbol{D}u \tag{3.42}$$

The equations for the state space derivatives can be written as:

$$\dot{q}_1 = \dot{x}_b = q_3 \tag{3.43}$$

$$\dot{q}_2 = \dot{\theta}_p = q_4 \tag{3.44}$$

$$\dot{q}_3 = \ddot{x}_b = \frac{1}{(m_b + m_p)}\left[-m_p\ell_p\dot{q}_4 - k_sq_1\right] \tag{3.45}$$

$$\dot{q}_4 = \ddot{\theta}_p = \frac{1}{(J_p + m_p\ell_p^2)}\left[-m_p\ell_p\dot{q}_3 + m_pg\ell_pq_2 + \frac{\eta_gK_g\eta_mk_tk_mV_m}{R_m} - \frac{\eta_gK_g^2\eta_mk_tk_mq_4}{R_m}\right] \tag{3.46}$$

Note that both Equation (3.45) and Equation (3.46) have the derivative of a state variable on the right-hand side which should be removed by manipulation. After substitution, the derivatives become:

$$\dot{q}_1 = \dot{x}_b = q_3 \tag{3.47}$$

$$\dot{q}_2 = \dot{\theta}_p = q_4 \tag{3.48}$$

$$
\begin{aligned}
\dot{q}_3 = \ddot{x}_b = {} & \frac{-(J_p + m_p\ell_p^2)R_mk_sq_1}{(m_mJ_p + J_pm_p + m_pl_p^2m_m)R_m} - \frac{m_p^2\ell_p^2gq_2}{(m_mJ_p + J_pm_p + m_pl_p^2m_m)R_m} \\
& + \frac{\eta_gK_g^2\eta_mk_tk_mm_p\ell_pq_4}{(m_mJ_p + J_pm_p + m_pl_p^2m_m)R_m} - \frac{\eta_gK_g\eta_mk_tm_p\ell_pV_m}{(m_mJ_p + J_pm_p + m_pl_p^2m_m)R_m}
\end{aligned} \tag{3.49}
$$

$$
\begin{aligned}
\dot{q}_4 = \ddot{\theta}_p = {} & \frac{R_mm_p\ell_pk_sq_1}{(m_mJ_p + J_pm_p + m_pl_p^2m_m)R_m} + \frac{m_pg\ell_p(m_m + m_p)q_2}{(m_mJ_p + J_pm_p + m_pl_p^2m_m)R_m} \\
& - \frac{\eta_gK_g^2\eta_mk_tk_m(m_m + m_p)q_4}{(m_mJ_p + J_pm_p + m_pl_p^2m_m)R_m} + \frac{\eta_gK_g\eta_mk_t(m_m + m_p)V_m}{(m_mJ_p + J_pm_p + m_pl_p^2m_m)R_m}
\end{aligned} \tag{3.50}
$$

Then the state-space matrices can be written as:

$$
A = \begin{bmatrix}
0 & 0 & 1 & 0 \\
0 & 0 & 0 & 1 \\
\dfrac{-(J_p + m_p\ell_p^2)k_s}{(m_mJ_p + J_pm_p + m_pl_p^2m_m)} & \dfrac{-m_p^2\ell_p^2g}{(m_mJ_p + J_pm_p + m_pl_p^2m_m)} & 0 & \dfrac{\eta_gK_g^2\eta_mk_tk_mm_p\ell_p}{(m_mJ_p + J_pm_p + m_pl_p^2m_m)R_m} \\
\dfrac{m_p\ell_pk_s}{(m_mJ_p + J_pm_p + m_pl_p^2m_m)} & \dfrac{m_pg\ell_p(m_m + m_p)}{(m_mJ_p + J_pm_p + m_pl_p^2m_m)} & 0 & \dfrac{-\eta_gK_g^2\eta_mk_tk_m(m_m + m_p)}{(m_mJ_p + J_pm_p + m_pl_p^2m_m)R_m}
\end{bmatrix} \tag{3.51}
$$

$$B = \begin{bmatrix} 0 \\ 0 \\ \dfrac{\eta_g K_g^2 \eta_m k_t k_m m_p \ell_p}{(m_m J_p + J_p m_p + m_p l_p^2 m_m) R_m} \\ \dfrac{-\eta_g K_g^2 \eta_m k_t k_m (m_m + m_p)}{(m_m J_p + J_p m_p + m_p l_p^2 m_m) R_m} \end{bmatrix} \tag{3.52}$$

$$C = \begin{bmatrix} 1 & 0 & 0 & 0 \\ 0 & 1 & 0 & 0 \end{bmatrix} \tag{3.53}$$

$$D = \begin{bmatrix} 0 \\ 0 \end{bmatrix} \tag{3.54}$$

With the parameters from Table 3.1, the state space matrices A and B become:

$$A = \begin{bmatrix} 0 & 0 & 1 & 0 \\ 0 & 0 & 0 & 1 \\ -33.2837894302619 & -0.400735294117647 & 0 & 0.193155294020131 \\ 58.1559082860322 & 17.8409548751007 & 0 & -8.59937952829350 \end{bmatrix} \tag{3.55}$$

$$B = \begin{bmatrix} 0 \\ 0 \\ -0.359402542463646 \\ 16.0007981233815 \end{bmatrix} \tag{3.56}$$

Now, the control gains can be computed using the following weighting matrices:

$$Q = \begin{bmatrix} 6200 & 0 & 0 & 0 \\ 0 & 28 & 0 & 0 \\ 0 & 0 & 22 & 0 \\ 0 & 0 & 0 & 1 \end{bmatrix} \tag{3.57}$$

$$R = 1 \tag{3.58}$$

Then the following control gains can be obtained:

$$k_{p,x} = -73.9623 , \text{ V/m} \tag{3.59}$$

$$k_{p,\theta} = 6.5227 , \text{ V/rad} \tag{3.60}$$

$$k_{d,x} = 5.2917 , \text{ V/(m/s)} \tag{3.61}$$

$$k_{d,\theta} = 1.1055 , \text{ V/(rad/s)} \tag{3.62}$$

Note that the final weighting matrices utilized in Equation (3.57) and Equation (3.58) are updated through trial and error and selected based on controller performance characteristics.

3.4 Deflection Signal Conditioning

The deflection from the flexible beam is computed based on a signal measured from a strain gauge. Flexible beam deflections change the electrical resistance of the strain gauge, which in turn changes the voltage measured across the strain gauge leads. The signal conditioning board secured to the experimental setup uses an amplifier is used to boost the difference in voltage to a higher level of electrical signal amplitude. This deflection signal is further fine tuned by two potentiometers, which allow for adjustment of output signal gain and offset. A low-pass filter is utilized to remove some noise from the sensor output signal, effectively giving the state space variables in the following form:

$$
\boldsymbol{q}_f = \begin{bmatrix} q_{1,f} \\ q_{2,f} \\ q_{3,f} \\ q_{4,f} \end{bmatrix} = \begin{bmatrix} H_1(s)x_b(s) \\ \theta_p(s) \\ H_1(s)\dot{x}_b(s) \\ H_2(s)\dot{\theta}_p(s) \end{bmatrix}
\tag{3.63}
$$

where $H_1(s)$ and $H_2(s)$ are 2nd order Butterworth filters with cutoff frequencies ω_{cf1} and ω_{cf2} respectively. Note that the angular position of the rigid bar is determined from a digital encoder output, and as such does not require filtering for noise reduction. Both cutoff frequencies are selected such that high-frequency components could be removed from the signal output. In the case of beam deflection, the cutoff frequency is selected to be twice the natural frequency of the beam, in order to remove some higher-order harmonics from the analog signal. In the case of the angular position rate of change, a large static value is selected. As such, the cutoff frequencies are calculated as follows:

$$
\omega_{cf1} = 2\omega_n \text{ , rad/sec}
\tag{3.64}
$$

$$
\omega_{cf2} = 10\pi \text{ , rad/sec}
\tag{3.65}
$$

where ω_n is the natural frequency of the flexible beam, which can be determined experimentally by manually perturbing the flexible beam and performing a FFT spectrum analysis.

The result of this analysis is shown in Figure 3.4(b). As such, the natural frequency is calculated as:

$$
\omega_n = 2\pi \cdot (1.2987) \text{ , rad/sec}
\tag{3.66}
$$

(a)

(b)
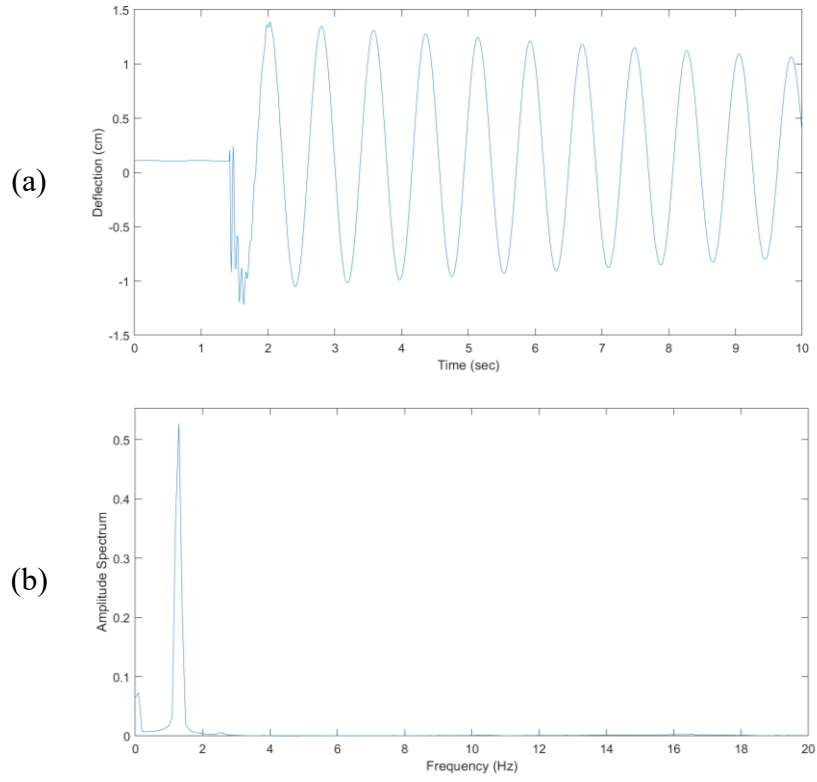
Figure 3.4: Determining the natural frequency of the flexible beam experimentally: (a) flexible beam response to perturbation, (b) frequency spectrum analysis of the perturbation.

Due to the prevalence of high-frequency components in the measured deflection signal, an updated signal conditioning board is proposed and ordered from Quanser for installation to the experimental setup. The original signal conditioning board in Figure 3.5(a) consisted primarily of resistors and a single amplifier to generate an output signal. The updated board in Figure 3.5(b) has incorporated several decoupling capacitors, voltage references, and an additional amplifier. The decoupling capacitors will result in a reduction in noise in the measured signal while the use of voltage references can improve data resolution [100].

(a)

(b)
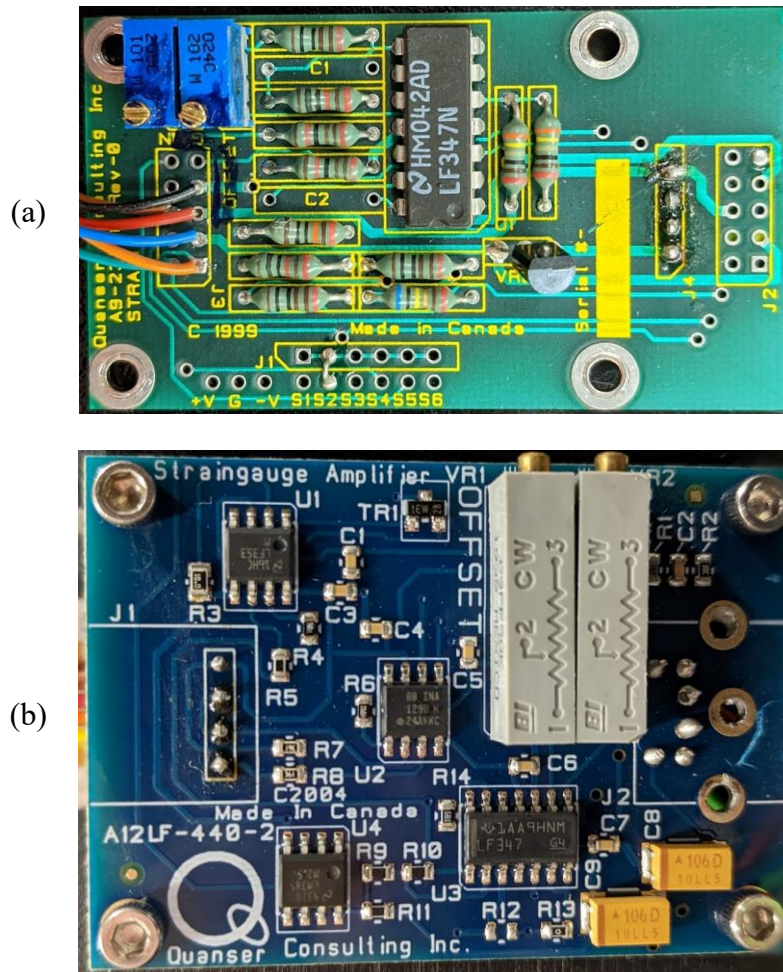
Figure 3.5: Signal conditioning boards utilized with the experimental setup: (a) the original signal conditioning board, (b) the updated signal conditioning board.

Further, the original stain gauge that was adhered to the flexible beam was replaced. The original strain gauge was adhered to the flexible beam using epoxy, leading to some high frequency noise due to the deterioration of the adhesive over time, particularly in response to the cumulative effect of humidity [101], as illustrated in Figure 3.6(a). A new dual-grid half-bridge strain gauge

is installed to a prepared surface via the cellophane tape method. As illustrated in Figure 3.6(b), the cumulative effect of the new signal conditioning board and the strain gauge is clear, in which the high frequency components previously found in the steady state solution space are eliminated for experimental procedures.
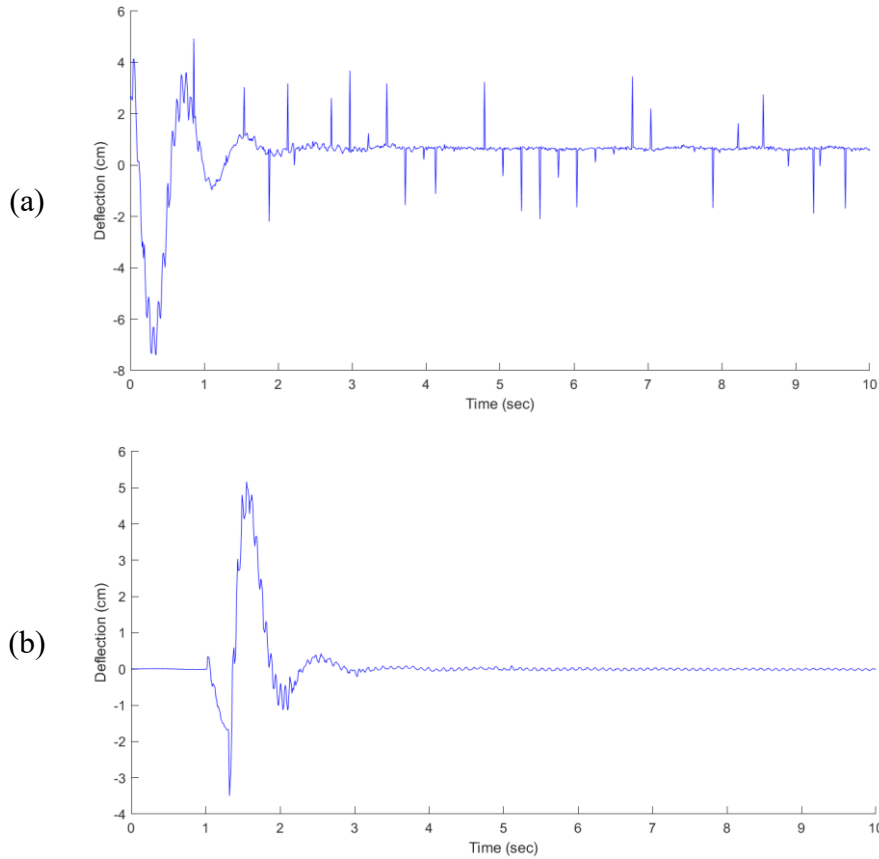
Figure 3.6: Comparison of deflection signals: (a) deflection signal using the old signal conditioning board and strain gauge, (b) deflection signal using the new signal conditioning board and strain gauge.

3.5 NF Controller Architecture

A NF controller is developed to compensate for nonlinear motions exhibited by the flexible beam. Consider a NF system with n input variables $\{x_1, x_2, \dots, x_n\}$ and one output z, the fuzzy rules can be represented with the following general form [102]:

$$\mathcal{R}_j: \text{If } \left(x_1 \text{ is } A_1^g\right) \text{ and } \left(x_2 \text{ is } A_2^g\right) \dots \text{ and } \left(x_n \text{ is } A_n^g\right)$$

$$\text{then } (z = b_0 + b_1^g x_1 + \dots + b_n^g x_n)$$

(3.67)

where A_i^g is a membership function (MF); $i = 1, 2, \ldots, n$, $g = 1, 2, \ldots, G$; G is the number of MF for each input, j is the number of fuzzy rules, and $b_0, b_1, \ldots, b_n$ are constants.
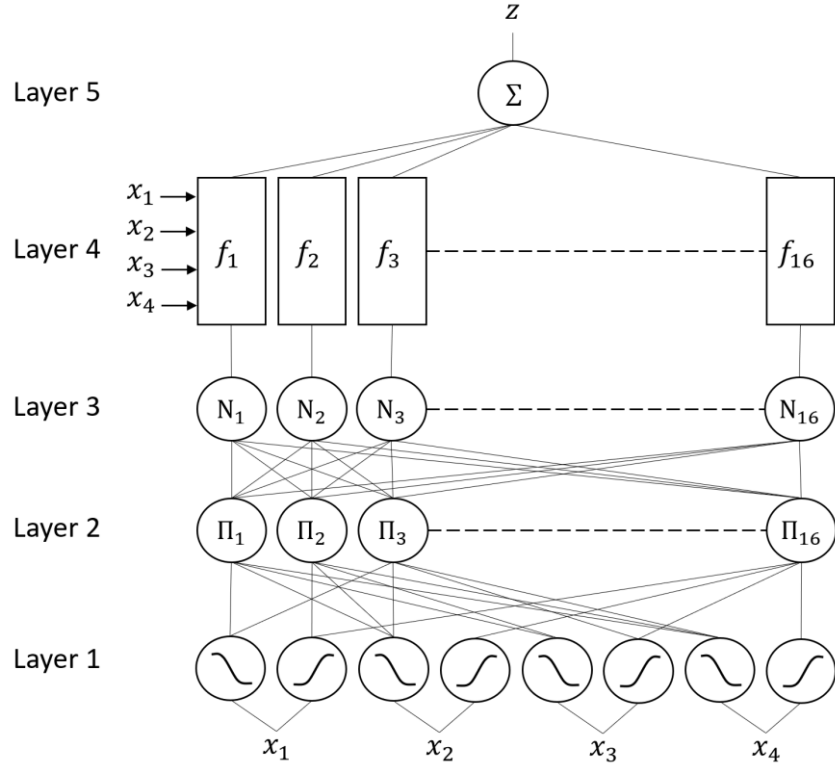
Figure 3.7: Architecture of the NF controller.

The network architecture of the developed NF system is shown in Figure 3.7. It has five layers with unity link weights. For simplicity, consider four inputs $\{x_1, x_2, x_3, x_4\}$, which represent four system states: $\{x_b, \theta_p, \dot{x}_b, \dot{\theta}_p\}$, respectively, where x_b is the deflection of the flexible beam, θ_p is the angular position of the pendulum arm, $\dot{x}_b$ is the deflection velocity of the flexible beam, and $\dot{\theta}_p$ is the angular velocity of the pendulum arm. The inputs are fuzzified in Layer 1 using two sigmoid MFs, negative large and positive large, with the following form:

$$\mu_n(x_i) = \frac{1}{1 + \exp\left[-a_J(x_i - c_J)\right]} \tag{3.68}$$

where x_i corresponds to a single input from $\{x_1, x_2, x_3, x_4\}$; a_J and c_J represent nonlinear parameters; $J = 1, 2, \ldots, 8$, $n = 1$ for negative large, and $n = 2$ for positive large.

The firing strength of each fuzzy rule is computed in Layer 2 by using a T-norm operator. If a product operator is used, then:

$$w_j = \mu_n(x_1) \times \mu_n(x_2) \times \mu_n(x_3) \times \mu_n(x_4) \tag{3.69}$$

where $j = 1, 2, \dots, 16$ and $n = 1, 2$.

The firing strength are normalized in Layer 3, or:

$$N_j = \frac{w_j}{\sum_{k=1}^{K} w_k} \tag{3.70}$$

where K is the total number of fuzzy rules.

If centroid defuzzification is performed in Layer 4 the control output z will be:

$$z = \sum_{j=1}^{K} N_j(p_j x_1 + q_j x_2 + r_j x_3 + s_j x_4 + t_j) \tag{3.71}$$

where p_j, q_j, r_j, s_j, and t_j are consequent linear parameters. The linear and nonlinear parameters of the NF controller will be trained by using the hybrid training technique outlined in Chapter 4.

Chapter 4

Optimization of the NF Controller

4.1 BPSO-based System Training

The linear and nonlinear NF parameters should be trained properly to optimize the mapping from the input space to the control output space. In this work, a novel hybrid training technique based on bisection particle swarm optimization (BPSO) is proposed for system training. System training is performed in two passes for all training data pairs propagated through the NF controller. In general, the training data pairs should be at least 5-times the number of linear data points to be optimized [102]. In the forward pass the nonlinear parameters are fixed, and the linear parameters are updated using the least-squares estimator (LSE). In the backward pass the linear parameters are fixed, and the non-linear parameters search area is updated using BPSO.

4.1.1 BPSO-based Nonlinear Parameter Training

Heuristic training algorithms can approach global minimums in optimization problems but are computationally expensive. To address this issue a particle swarm optimization technique is integrated with the computationally efficient bisection method to incrementally optimize the nonlinear membership function (MF) parameters. The algorithm works by spanning a solution space across each nonlinear parameter to be optimized. The upper boundary $\mathcal{B}_u$ and lower boundary $\mathcal{B}_l$ of the solution space are initialized:

$$\mathcal{B}_{u,0} = b_0 + \delta \tag{4.1}$$

$$\mathcal{B}_{l,0} = b_0 - \delta \tag{4.2}$$

where b_0 is a generalized variable representing the initial value of the nonlinear parameter to be optimized, and δ is a parameter representing the width of one-half of the solution space.

In the experimental procedure outlined in this work, the width is based on the product of a random value and a percentage (γ) of the magnitude of the initial nonlinear parameter:

$$\delta = \text{rand}(\gamma \cdot b_0) \tag{4.3}$$

In experimental procedures a percentage of 50% is used for training operations.

For each propagated training data pair, the NF system output is concurrently computed for upper boundary particle y_u and the lower boundary particle y_l. The respective error of each particle is calculated by comparing it to y_d, the desired NF output will be:

$$\varepsilon_u = |y_u - y_d| \tag{4.4}$$

$$\varepsilon_l = |y_l - y_d| \tag{4.5}$$

Based on the magnitude of the calculated error, the corresponding boundary particle is bisected as:

$$\mathcal{B}_{u,i+1} = \begin{cases} \mathcal{B}_{u,i} - \left| \dfrac{\mathcal{B}_{u,i} - \mathcal{B}_{l,i}}{2} \right| & \text{if } \varepsilon_u \geq \varepsilon_l \\ \mathcal{B}_{u,i} & \text{otherwise} \end{cases} \tag{4.6}$$

$$\mathcal{B}_{l,i+1} = \begin{cases} \mathcal{B}_{u,i} - \left| \dfrac{\mathcal{B}_{u,i} - \mathcal{B}_{l,i}}{2} \right| & \text{if } \varepsilon_u < \varepsilon_l \\ \mathcal{B}_{l,i} & \text{otherwise} \end{cases} \tag{4.7}$$

This process is repeated iteratively until the difference between boundary particles becomes sufficiently small:

$$\left| \mathcal{B}_{u,i} - \mathcal{B}_{l,i} \right| < \varepsilon_{min} \tag{4.8}$$

In experimental procedures, the stopping criteria is selected as $\varepsilon_{min} = 10^{-6}$. This ensures several training iterations are performed, and training operation do not immediately conclude in instances where δ is small.

Figure 4.1 shows a flowchart indicating the main algorithm procedures. To begin, the upper and lower boundary particles for each nonlinear parameter are initialized using Equation (4.1) and Equation (4.2), respectively. Each nonlinear parameter is assigned a randomized index, which is incremented by a prime number every iteration loop. Since parameters are optimized individually, the BPSO will use different starting points so as to ensure the parameter sequencing is unique between program loops. Next, the flexible beam deflection data is measured, and the NF controller output y_d is computed. NF controller outputs are determined utilizing the upper (y_u) and lower (y_l) boundary particles, respectively. Using Equation (4.4) and Equation (4.5), the error between the NF controller outputs is computed. The boundary particle with a larger magnitude error is bisected, halving the distance between the respective boundary particle and the initial value to

optimize the nonlinear parameters using Equation (4.6) or Equation (4.7). The boundary particle with the small magnitude remains unchanged. The error between each boundary particles position is compared using Equation (4.8); the process is repeated for the next nonlinear parameter by incrementing the nonlinear parameter index, until the stopping criteria are met. The optimization operation is terminated once the distance between boundary particles is less than the threshold.
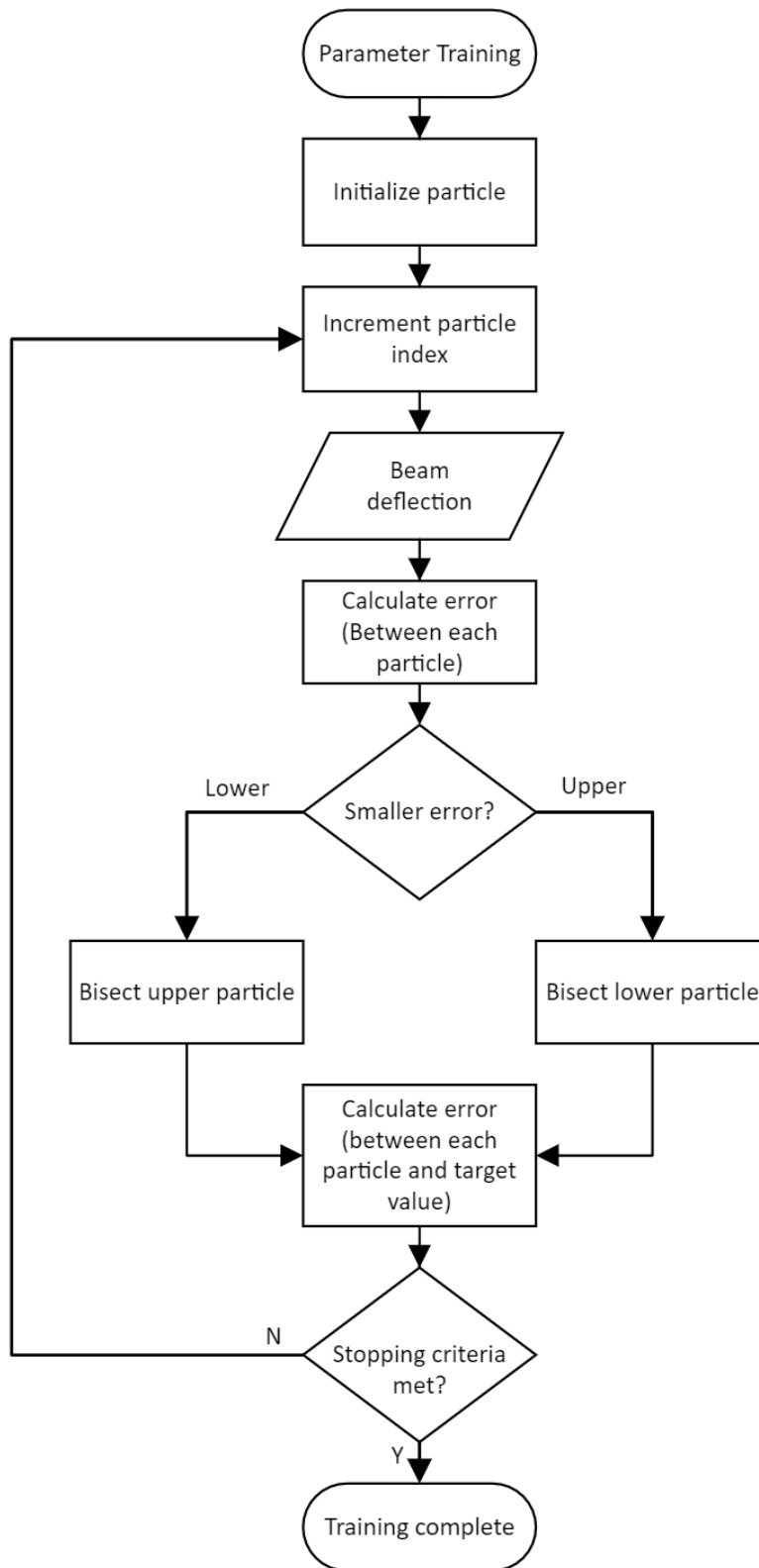
Figure 4.1: Flowchart of the nonlinear parameter training algorithm methodology.

4.1.2 LSE for Linear Parameter Training

The LSE is used to optimize the linear parameters of the proposed NF controller, by minimizing the objective function or minimizing the errors between the desired system outputs and calculated system outputs. Consider the outputs generated by a NF controller:

$$\theta_1 f_1(\boldsymbol{u}) + \theta_2 f_2(\boldsymbol{u}) + \cdots + \theta_n f_n(\boldsymbol{u}) = y \tag{4.9}$$

where $\boldsymbol{u}$ are the NF controller inputs $\{x_1, x_2, \ldots, x_n\}$; $\boldsymbol{\theta} = \{\theta_1, \theta_2, \ldots, \theta_n\}$ corresponds to the unknown linear parameters, $\{f_1, f_2, \ldots, f_n\}$ are the nodal outputs from Layer 4 of the NF controller as illustrated in Figure 3.7; and y is the NF controller output. A generalized representation of Equation (4.9) can be written as:

$$
\begin{array}{ccccccccc}
f_1(\boldsymbol{u_1})\theta_1 & + & f_2(\boldsymbol{u_1})\theta_2 & + & \cdots & + & f_n(\boldsymbol{u_1})\theta_n & = & y_1 \\
f_1(\boldsymbol{u_2})\theta_1 & + & f_2(\boldsymbol{u_2})\theta_2 & + & \cdots & + & f_n(\boldsymbol{u_2})\theta_n & = & y_2 \\
\vdots & & \vdots & & \vdots & & \vdots & & \vdots \\
f_1(\boldsymbol{u_m})\theta_1 & + & f_2(\boldsymbol{u_m})\theta_2 & + & \cdots & + & f_n(\boldsymbol{u_m})\theta_n & = & y_m
\end{array}
\tag{4.10}
$$

where $\boldsymbol{u_j}$ are the NF controller inputs corresponding to the jth training data pair for $j = 1, 2, \ldots, m$, m is the number of training data pairs, and n is the number of linear parameters to be optimized. The matrix representation of Equation (4.10) becomes:

$$
\begin{bmatrix}
f_1(\boldsymbol{u_1}) & f_2(\boldsymbol{u_1}) & \cdots & f_n(\boldsymbol{u_1}) \\
f_1(\boldsymbol{u_2}) & f_2(\boldsymbol{u_2}) & \cdots & f_n(\boldsymbol{u_2}) \\
\vdots & \vdots & & \vdots \\
f_1(\boldsymbol{u_m}) & f_2(\boldsymbol{u_m}) & \cdots & f_n(\boldsymbol{u_m})
\end{bmatrix}
\begin{bmatrix}
\theta_1 \\ \theta_2 \\ \vdots \\ \theta_n
\end{bmatrix}
=
\begin{bmatrix}
y_1 \\ y_2 \\ \vdots \\ y_m
\end{bmatrix}
\tag{4.11}
$$

Equation (4.11) can be simplified as:

$$\mathcal{A}\boldsymbol{\theta} = \boldsymbol{y} \tag{4.12}$$

Thus, the error between desired and calculated NF outputs can be rewritten as:

$$\boldsymbol{e} = \boldsymbol{y} - \mathcal{A}\boldsymbol{\theta} \tag{4.13}$$

Then the objective function will be:

$$E(\boldsymbol{\theta}) = \frac{1}{2}(y_1 - \boldsymbol{a}_1^{\mathrm{T}}\boldsymbol{\theta})^2 + \cdots + \frac{1}{2}(y_i - \boldsymbol{a}_i^{\mathrm{T}}\boldsymbol{\theta})^2 + \cdots + \frac{1}{2}(y_m - \boldsymbol{a}_m^{\mathrm{T}}\boldsymbol{\theta})^2 \tag{4.14}$$

$$= \frac{1}{2}\sum_{i=1}^{m}(y_i - \boldsymbol{a}_i^{\mathrm{T}}\boldsymbol{\theta})^2 \tag{4.15}$$

where $\boldsymbol{a_1}, ..., \boldsymbol{a_m}$ is a row from matrix $\mathcal{A}$, as denoted by its subscript. The error for each training data pair can be written as:

$$e_i = y_i - \boldsymbol{a}_i^{\mathrm{T}}\boldsymbol{\theta}; \ i = 1, 2, ..., m. \tag{4.16}$$

Thus, the objective function in Equation (4.14) can be further simplified to:

$$E(\boldsymbol{\theta}) = \boldsymbol{e}_1^{\mathrm{T}}\boldsymbol{e}_1 + \boldsymbol{e}_2^{\mathrm{T}}\boldsymbol{e}_2 + ... + \boldsymbol{e}_i^{\mathrm{T}}\boldsymbol{e}_i + \cdots + \boldsymbol{e}_m^{\mathrm{T}}\boldsymbol{e}_m \tag{4.17}$$

$$E(\boldsymbol{\theta}) = \sum_{i=1}^{m} \boldsymbol{e}_i^{T}\boldsymbol{e}_i \tag{4.18}$$

$$E(\boldsymbol{\theta}) = \boldsymbol{e}^{\mathrm{T}}\boldsymbol{e} \tag{4.19}$$

Consider:

$$\boldsymbol{e}^{\mathrm{T}}\boldsymbol{e} = (\boldsymbol{y} - \mathcal{A}\boldsymbol{\theta})^{\mathrm{T}}(\boldsymbol{y} - \mathcal{A}\boldsymbol{\theta}) \tag{4.20}$$

Then:

$$E(\boldsymbol{\theta}) = [\boldsymbol{y}^{\mathrm{T}} - (\mathcal{A}\boldsymbol{\theta})^{\mathrm{T}}](\boldsymbol{y} - \mathcal{A}\boldsymbol{\theta}) \tag{4.21}$$

$$E(\boldsymbol{\theta}) = [\boldsymbol{y}^{\mathrm{T}} - \boldsymbol{\theta}^{\mathrm{T}}\mathcal{A}^{\mathrm{T}}](\boldsymbol{y} - \mathcal{A}\boldsymbol{\theta}) \tag{4.22}$$

$$E(\boldsymbol{\theta}) = \boldsymbol{y}^{\mathrm{T}}\boldsymbol{y} - \boldsymbol{y}^{\mathrm{T}}\mathcal{A}\boldsymbol{\theta} - \boldsymbol{\theta}^{\mathrm{T}}\mathcal{A}^{\mathrm{T}}\boldsymbol{y} + \boldsymbol{\theta}^{\mathrm{T}}\mathcal{A}^{\mathrm{T}}\mathcal{A}\boldsymbol{\theta} \tag{4.23}$$

Consider the transpose of $\boldsymbol{y}$ from Equation (4.12):

$$\boldsymbol{y}^{\mathrm{T}} = (\mathcal{A}\boldsymbol{\theta})^{\mathrm{T}} \tag{4.24}$$

$$\boldsymbol{y}^{\mathrm{T}} = \boldsymbol{\theta}^{\mathrm{T}}\mathcal{A}^{\mathrm{T}} \tag{4.25}$$

Using Equations (4.12) and (4.25), Equation (4.23) becomes:

$$E(\boldsymbol{\theta}) = \boldsymbol{y}^{\mathrm{T}}\boldsymbol{y} - \boldsymbol{y}^{\mathrm{T}}\mathcal{A}\boldsymbol{\theta} - \boldsymbol{y}^{\mathrm{T}}\mathcal{A}\boldsymbol{\theta} + \boldsymbol{\theta}^{\mathrm{T}}\mathcal{A}^{\mathrm{T}}\mathcal{A}\boldsymbol{\theta} \tag{4.26}$$

$$E(\boldsymbol{\theta}) = \boldsymbol{y}^{\mathrm{T}}\boldsymbol{y} - 2\boldsymbol{y}^{\mathrm{T}}\mathcal{A}\boldsymbol{\theta} + \boldsymbol{\theta}^{\mathrm{T}}\mathcal{A}^{\mathrm{T}}\mathcal{A}\boldsymbol{\theta} \tag{4.27}$$

Using the general forms listed in Appendix C, the objective function from Equation (4.27) can be minimized with respect to the vector of the linear parameters to be optimized:

$$\frac{\partial E(\boldsymbol{\theta})}{\partial \boldsymbol{\theta}} = \frac{\partial (\boldsymbol{y}^{\mathrm{T}}\boldsymbol{y})}{\partial \boldsymbol{\theta}} - \frac{2\boldsymbol{y}^{\mathrm{T}}\mathcal{A}\boldsymbol{\theta}}{\partial \boldsymbol{\theta}} + \frac{\boldsymbol{\theta}^{\mathrm{T}}\mathcal{A}^{\mathrm{T}}\mathcal{A}\boldsymbol{\theta}}{\partial \boldsymbol{\theta}} \tag{4.28}$$

$$\frac{\partial E(\boldsymbol{\theta})}{\partial \boldsymbol{\theta}} = 0 - 2\mathcal{A}^\mathrm{T}\boldsymbol{y} + [\mathcal{A}^\mathrm{T}\mathcal{A} + (\mathcal{A}^\mathrm{T}\mathcal{A})^\mathrm{T}]\boldsymbol{\theta} \tag{4.29}$$

$$\frac{\partial E(\boldsymbol{\theta})}{\partial \boldsymbol{\theta}} = -2\mathcal{A}^\mathrm{T}\boldsymbol{y} + 2\mathcal{A}^\mathrm{T}\mathcal{A}\boldsymbol{\theta} \tag{4.30}$$

Let:

$$\frac{\partial E(\boldsymbol{\theta})}{\partial \boldsymbol{\theta}} = 0 \tag{4.31}$$

Then Equation (4.30) can be simplified to:

$$2\mathcal{A}^\mathrm{T}\boldsymbol{y} = 2\mathcal{A}^\mathrm{T}\mathcal{A}\boldsymbol{\theta} \tag{4.32}$$

which yields the following expression to optimize the linear NF parameters:

$$\boldsymbol{\theta} = (\mathcal{A}^\mathrm{T}\mathcal{A})^{-1}\mathcal{A}^\mathrm{T}\boldsymbol{y} \tag{4.33}$$

4.2 NF Output Oscillation Suppression

Another means of the developed NF controller is to reduce the high frequency oscillations in the steady state solution space in the flexible structure. Firstly, the system is modeled as a simplified mass-spring-damper system, as illustrated in Figure 4.2. When this system is perturbed, a restoring force will act on the flexible structure to return it to its equilibrium position. The magnitude of the restoring force and the consequent control action is directly proportional to the deflection of the flexible structure.
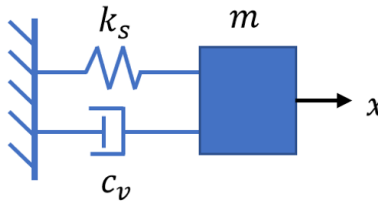

Figure 4.2: Simplified mass-spring-damper model.

Based on the simple mass-spring-damper model with a discrete mass node in Figure 4.2, the restoring force can be represented as a combination of the spring and damping force [103]:

$$f_r(x, \dot{x}) = k_s x + c_v \dot{x} \tag{4.34}$$

However, variations in control action are observed in experimental procedures when the system state is close to its equilibrium, suggesting a dependence on more than position and velocity. These problems were also observed in literature where it was found that the restoring force of flexible structures exhibited nonlinear characteristics at higher velocities [104]. To tackle this problem without further system parameterization, a dynamic output suppression technique is proposed in this work to reduce the control action of the controller when nonlinear variations are more prevalent. First, consider the following Gaussian MF:

$$\mu_{E1}(x_1) = \exp\left[-\frac{1}{2}\frac{(x_1 - c)^2}{\lambda \cdot \sigma^2}\right] \tag{4.35}$$

where x_1 is the NF input corresponding to flexible beam deflection, c is the center of the MF, and σ is the standard deviation. The parameter λ is based on data acquired during the hybrid training process, and is expressed as:

$$\lambda = \frac{\text{deflection undershoot}}{\text{deflection overshoot}} \tag{4.36}$$

In this application the deflection overshoot and undershoot are defined as the first and second deflection minima in response to system perturbation. Consider the complement of Equation (4.35):

$$\mu_{E_2}(x_1) = 1 - \mu_{E_1}(x_1) \tag{4.37}$$

A continuous fuzzy boundary function can be formulated by utilizing the max S-norm (T-conorm) operator of the fuzzy set E_1 and its complement:

$$\mu_{E_3}(x_1) = \mu_{E_1}(x_1) \vee \mu_{E_2}(x_1) \tag{4.38}$$

By concurrently updating the fuzzy boundary function during NF parameter training, the range of beam deflection inputs corresponding to a limited controller response can be adjusted adaptively. The width of the range of inputs will be narrower when the difference between the deflection overshoot and undershoot is smaller. Conversely, the range will be wider when the difference is larger. Figure 4.3(a) shows the MFs of E_1 and E_2, and their associated boundary function E_3 is depicted in Figure 4.3(b).

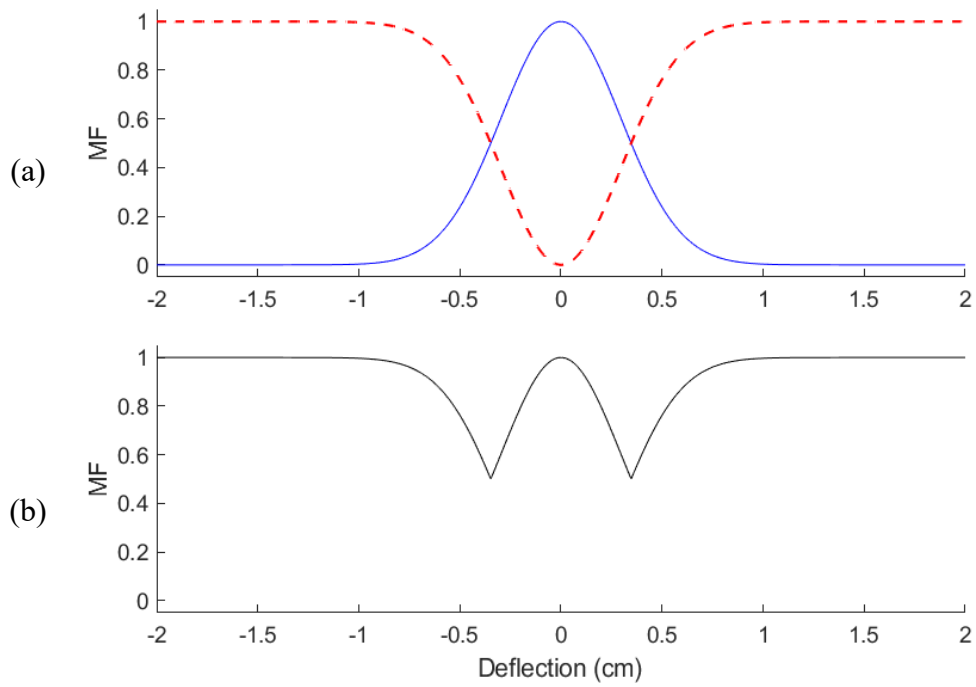The effectiveness of the developed NF control technology will be examined experimentally in Chapter 5.

Figure 4.3: (a) Fuzzy membership functions E_1 (solid line) and E_2 (dashed line), (b) fuzzy boundary function E_3.

Chapter 5
Control of a Flexible Structure with Dynamic Loading

5.1 Overview

To verify the effectiveness of the developed NF controller and hybrid training technique, a series of experimental tests are conducted using the apparatus as described in Figure 5.2. Each test begins with a "swing-up" procedure, where the rigid bar is balanced above the flexible beam until a stable solution is achieved. Then, a time-limited voltage is provided to the DC motor to drive the rigid bar to perturb the flexible structure. Instead of applying a perturbation, a time-limited perturbation signal is used to accommodate variations in the initial deflection of the flexible structure. After applying the perturbation signal, the controller is activated to suppress the vibrations to achieve a steady state solution. To examine the effectiveness of the developed control system (Controller-4), three related controllers are utilized in this testing procedure as follows:

1) Controller-1: A classical fuzzy controller without system training.

2) Controller-2: The proposed NF controller, trained using a hybrid method with least square estimator (LSE) and gradient decent (GD) algorithm.

3) Controller-3: The proposed NF controller, trained using a hybrid method with LSE and the proposed BPSO.

4) Controller-4: The proposed NF controller with output suppression, trained using a hybrid method with LSE and the proposed BPSO.

To prevent possible damage to the experimental setup, two limitations are integrated into each controller utilized in tests: a rotary bar angle watchdog and a control voltage saturation indicator. As the proposed NF controller is capable of responding to a wide range of input states, significant deflections will be met with a proportionally large control action. As such, in each instance of deflection signal measurement, the angle of the rigid bar will be compared to a "watchdog" angle, which is set to a preliminary value of ± 60 degrees from the vertical position. If the angle of the rigid bar exceeds the watchdog angle at any point in the experiment, a control voltage of 0 V is provided to the DC motor and the program is aborted. Similarly, to prevent damage to the DC motor, a limitation is placed on the control voltage. All generated control

voltages exceeding ± 6 V will be capped to ± 6 V. Figure 5.1 shows an example for illustration, which utilizes a saturated control voltage between 1.19 sec and 1.31 sec.
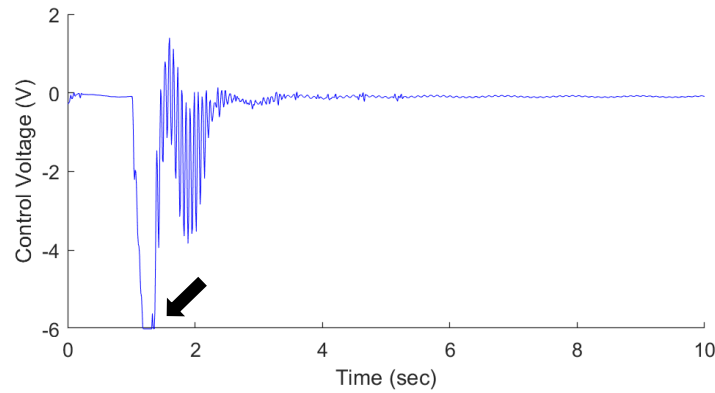
Figure 5.1: Illustration of the control voltage generated during experimental procedures. The control voltage saturation is indicated by the black arrow.

A performance comparison is made among the related controllers in terms of overshoot, undershoot, and settling time. Overshoot and undershoot are calculated based on the deviation from the mean steady state solution. Settling time is measured by placing a boundary around the mean steady state solution and recording the last instance where the beam deflection crosses the boundary. For all experimental procedures, a total boundary width of 0.2 cm is selected to accommodate the high frequency vibrations that remain in the steady state solution space.

A comparison between Controller-1 and Controller-2 is made to assess the feasibility of using a NF controller (i.e., NF vs a general fuzzy control) to suppress the vibrations of the flexible structure. Both Controller-2 and Controller-3 have the identical NF structure; but the test is to examine the effectiveness of the proposed BPSO training method in Controller-3, with respect to the classical GD algorithm utilized in Controller-2 to optimize the nonlinear controller parameters. Both Controller-3 and Controller-4 are trained using the same hybrid training method; the comparison is to examine the effectiveness of the proposed output suppression technique used in Controller-4 to reduce the vibrations induced during controller response.

5.2 Simulation of Dynamic Loading

Extra magnetic mass blocks are placed at different locations along the flexible beam to simulate the variable system dynamics. This test demonstrates the adaptability of the controllers in response to dynamic loading. Each mass block weighs 50 g; a pair of mass blocks are placed on

the opposite sides of the beam in each test as shown in Figure 5.2. The mass blocks are placed at one of three different locations, or zones, along the length of the flexible beam (as separated by yellow tapes). Each zone is about 1 inch wide. Zone 1 begins 2 inches from the top of the flexible beam, and Zones 2 and 3 are located with an additional 2 inches downward, respectively.
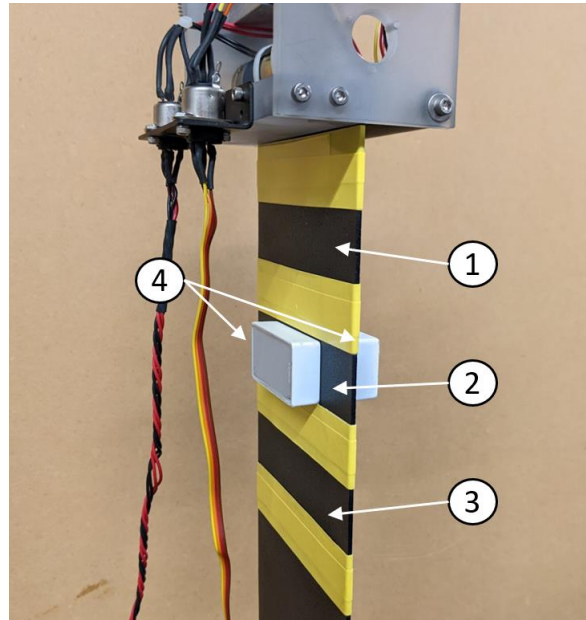
Figure 5.2: Dynamic loading test configurations: (1) Zone 1, (2) Zone 2, (3) Zone 3, (4) magnetic mass blocks

5.3 Experimental Result Analysis

The four controllers discussed in Section 5.1 are tested for four separate loading conditions: no additional mass blocks, 100 g of additional mass blocks on Zone 1, on Zone 2, and on Zone 3, respectively. In each instance, a plot is produced to show the deflection of the flexible beam in response to a perturbation, as well as the controller response with respect to the steady state solution. Each test is performed over a 10 sec. interval, but the x-axis of each plot is truncated to 2 sec. for clarity.

5.3.1 No Extra Mass Blocks

The deflection of the flexible beam during perturbation and control performance from the four tested controllers is shown in Figure 5.3. The related test results are summarized in Table 5.1. The listed percent changes in overshoot, undershoot and settling time, are relative to the performance results of the fuzzy controller (Controller-1). Clearly, NF controllers (Controllers 2-

4) outperform the classical fuzzy controller (Controller-1) due to proper system training. Although both Controller-2 and Controller-3 exhibit similar control characteristics, Controller-3 is able to achieve a 30.33% reduction in settling time compared to 20.22% reduction of Controller-2, due to the effective BPSO training strategy. On the other hand, Controller-4 performs even better than Controller-3 due to its efficient output suppression strategy in reducing overshoot, undershoot, settling time and the associated high frequency oscillations induced by control actions.
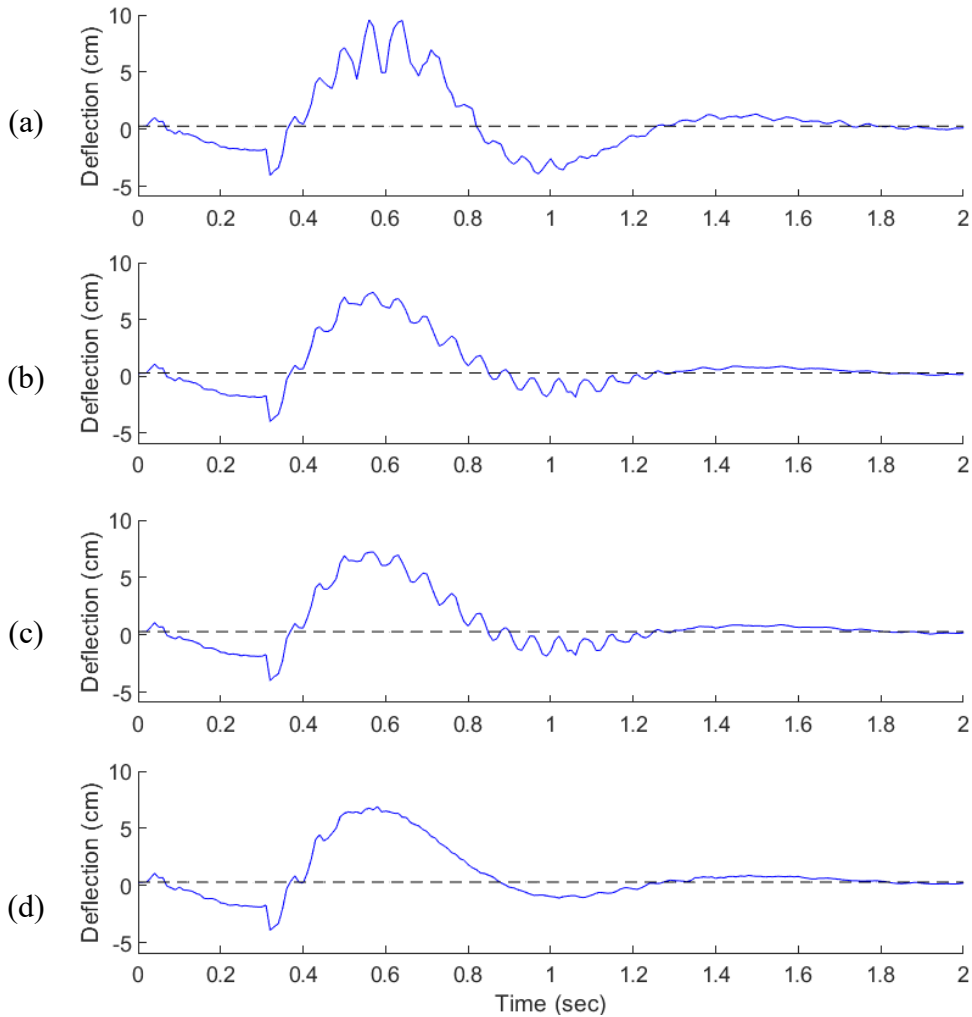
Figure 5.3: Deflection of the flexible beam using each controller: (a) Controller-1, (b) Controller-2, (c) Controller-3 (d) Controller-4.

Table 5.1: Experimental results, no additional mass blocks.

Controller	Overshoot (cm)	Percent Change	Undershoot (cm)	Percent Change	Settling Time (msec)	Percent Change
Controller-1	9.30	--	3.64	--	455	--
Controller-2	7.10	-23.66%	1.58	-56.59%	363	-20.22%
Controller-3	6.94	-25.38%	1.58	-56.59%	317	-30.33%
Controller-4	6.62	-28.82%	0.82	-77.47%	298	-34.51%

5.3.2 Additional Mass Blocks on Zone 1

Additional mass blocks are placed on Zone 1 of the flexible structure to simulate different beam dynamics. The performance of the related controllers is shown in Figure 5.4, and the results are summarized in Table 5.2. Similar trends can be observed as with the no load case, or NF controllers (Controllers 2-4) perform better than the fuzzy controller (Controller-1) due to training operations. With respect to Controller-1, Controller-3 has 10.08% reduction in settling time with the comparison of 0.42% reduction from Controller-2, due to the effective BPSO training that can recurrently update the nonlinear MF parameters and accommodate changing system dynamics. On the other hand, the developed Controller-4 outperforms other three controllers due to its superior high frequency oscillation suppression capability.
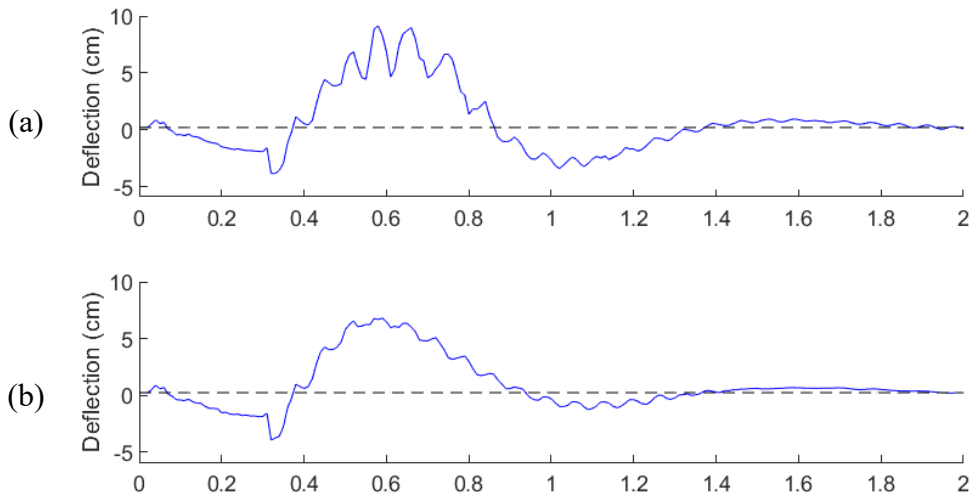
Figure 5.4: Deflection of the flexible beam with additional mass blocks on Zone 1 using different controllers: (a) Controller-1, (b) Controller-2, (c) Controller-3 (d) Controller-4.

Table 5.2: Experimental results, additional mass blocks on Zone 1.

Controller	Overshoot (cm)	Percent Change	Undershoot (cm)	Percent Change	Settling Time (msec)	Percent Change
Controller-1	8.93	--	3.19	--	238	--
Controller-2	6.56	-26.54%	1.02	-68.03%	237	-0.42%
Controller-3	6.50	-27.21%	1.07	-66.46%	214	-10.08%
Controller-4	6.30	-29.45%	0.85	-73.35%	190	-20.17%

5.3.3 Additional Mass Blocks on Zone 2

The mass blocks are placed to Zone 2 to simulate a different flexible beam dynamics. The performance of the related controllers is illustrated in Figure 5.5, and the results are summarized in Table 5.3. Controllers 2-4 perform better than Controller 1 due to training operations. Compared to Controller-1, both Controller-2 and Controller-3 have a reduction in settling time of 17.28% and 18.38%, respectively. Controller-3 is able to achieve superior results compared to Controller-2 due to the recurrent optimization of the nonlinear parameters through BPSO training, but the results are less significant compared to the loading case where the mass blocks are placed on Zone 1. Controller-4 performs even better than Controller-3 by coupling the proposed output suppression technique with the proposed BPSO training technique. As a result, the prevalence of high frequency oscillations in the steady state space is reduced, and an improved reduction in settling time of 21.69% is achieved.
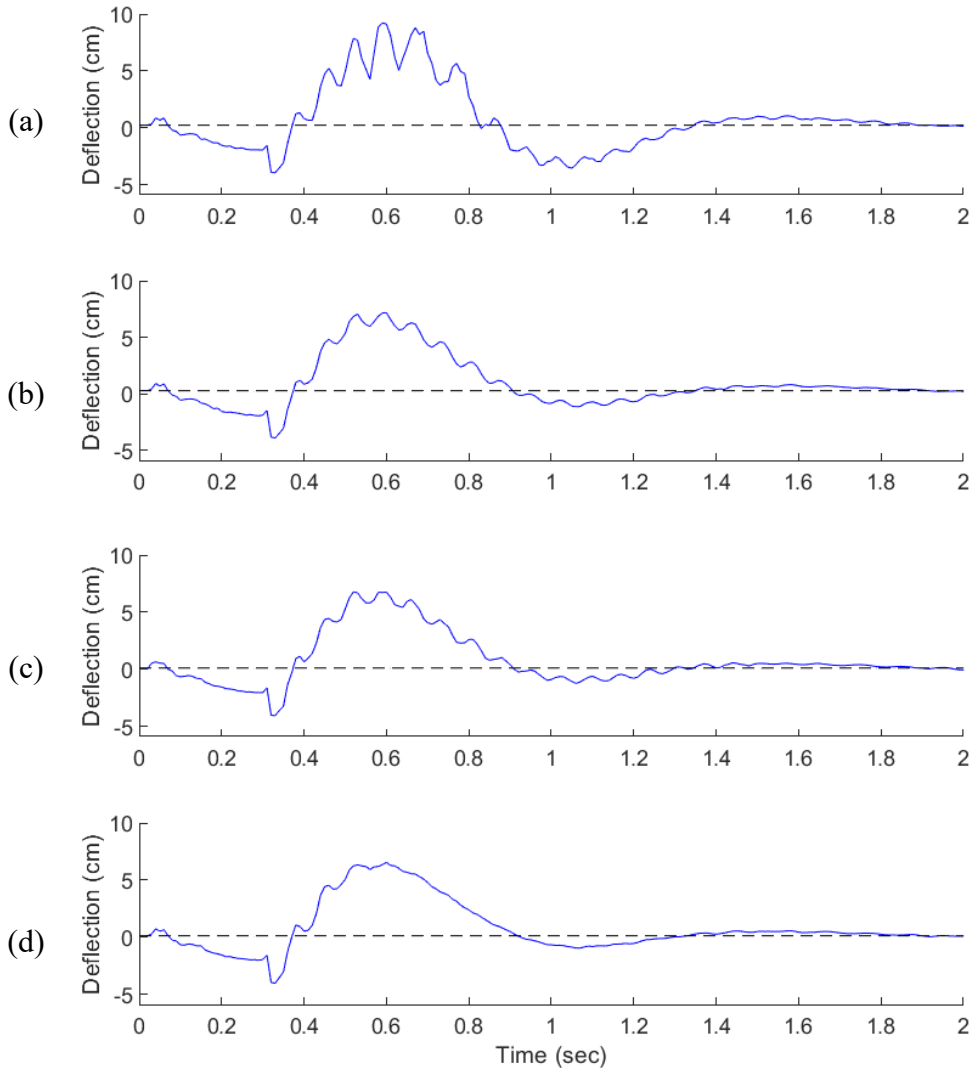
Figure 5.5: Deflection of the flexible beam with additional mass blocks on Zone 2 using different controllers: (a) Controller-1, (b) Controller-2, (c) Controller-3 (d) Controller-4.

Table 5.3: Experimental results, additional mass blocks on Zone 2.

Controller	Overshoot (cm)	Percent Change	Undershoot (cm)	Percent Change	Settling Time (msec)	Percent Change
Controller-1	8.99	--	3.33	--	272	--
Controller-2	6.98	-22.36%	1.01	-69.67%	225	-17.28%
Controller-3	6.66	-25.92%	1.13	-66.07%	222	-18.38%
Controller-4	6.42	-28.59%	0.83	-75.08%	213	-21.69%

5.3.4 Additional Mass Blocks on Zone 3

The flexible beam dynamics are changed by moving the mass blocks to Zone 3. The performance of each controller is shown in Figure 5.6, and the experimental results are summarized in Table 5.4. Similar to other experimental procedures, training operations allow Controllers 2-4 to achieve better results compared to Controller-1. When compared to Controller-1, Controller-2 and Controller-3 can reduce the settling time of 7.07% and 24.38% respectively. Controller-3 outperforms Controller-2 by recursively updating the nonlinear NF MF parameters using the proposed BPSO method. Controller-4 achieves better results compared to Controller-3 by utilizing the proposed output suppression technique, which can reduce the high frequency oscillations induced by control actions.
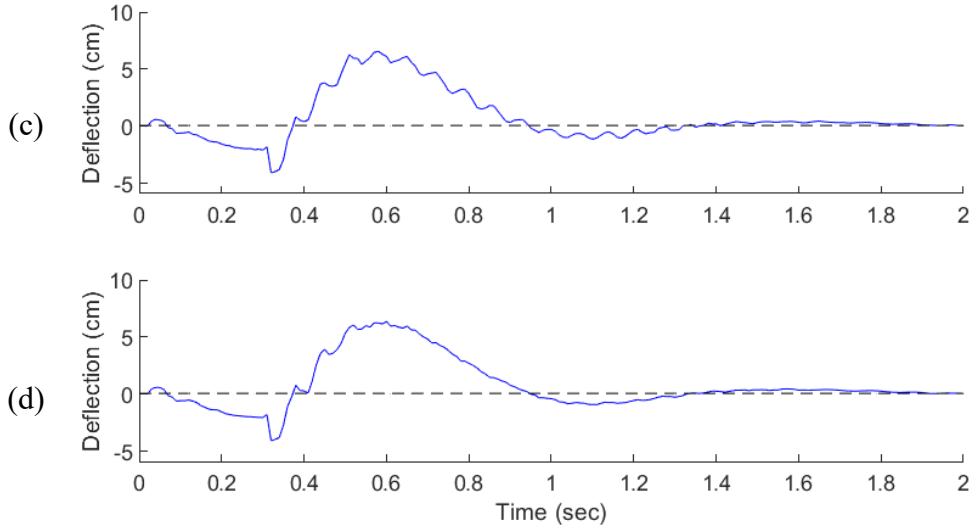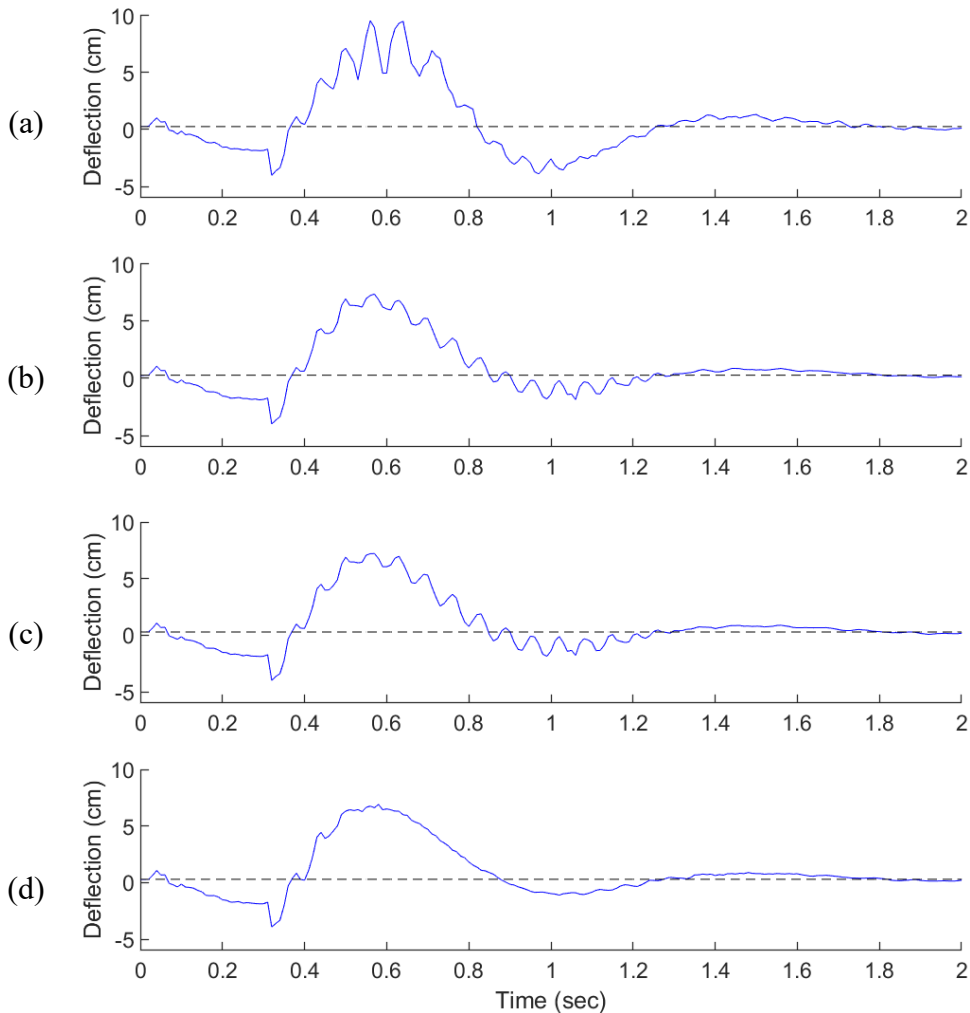

Figure 5.6: Deflection of the flexible beam with additional mass blocks on Zone 3 using different controllers: (a) Controller-1, (b) Controller-2, (c) Controller-3 (d) Controller-4.

Table 5.4: Experimental results, additional mass blocks on Zone 3.

Controller	Overshoot (cm)	Percent Change	Undershoot (cm)	Percent Change	Settling Time (msec)	Percent Change
Controller-1	9.01	--	3.86	--	283	--
Controller-2	7.09	-21.31%	1.11	-71.24%	263	-7.07%
Controller-3	7.03	-21.98%	1.16	-69.95%	214	-24.38%
Controller-4	6.68	-25.86%	0.87	-77.46%	204	-27.92%

Chapter 6
Conclusion and Future Work

6.1 Summary

In this thesis, the first objective is to develop a new type of an air-to-air refueling (AAR) system for commercial applications. A preliminary design of a probe-drogue AAR system has been developed for refueling helicopters from the FuelBoss. The preliminary design outlines the placement of AAR components, including the hose drum unit, within a 3D model. Simulations were performed to demonstrate the effectiveness of an active mass damping control technique. The design and simulation results have been approved from the Work Team including experts in this area, pilots, and business owners.

Since no real commercial application of AAR exists, a flexible beam experimental setup is selected to model the dynamic conditions of hose-drogue refueling dynamics. The second objective is to develop an adaptive neuro-fuzzy (NF) technology to suppress hose-drogue vibrations under variable dynamics conditions. The control operation is performed by a unique NF reasoning system. A new hybrid training technique based on the bisection particle swarm optimization (BPSO) algorithm is proposed to optimize the NF system parameters recursively to accommodate changes to system dynamics. Furthermore, to solve the issue of unstable control response to extra disturbances in the steady state solution space, a fuzzy boundary function is suggested to actively modulate the control signal. The effectiveness of the proposed NF controller and hybrid training method has been verified by systematic experimental tests under different system dynamics conditions by placing mass blocks at different locations on the flexible beam. Test results have shown that the proposed adaptive NF controller and hybrid training based on the BPSO method have clear advantages over the fuzzy control and the classical hybrid training algorithms, in terms of overshoot, undershoot, and settling time. Controller performance in the steady state solution space can be further improved when the suggested control suppression is applied.

6.2 Future Work

Due to the influence of the COVID pandemic and supply chain breakout, this MSc. project has to be limited to primary theoretical research utilizing available lab facilities, without verification using real AAR testing. Advanced research and development will be undertaken in the following aspects in the future:

1. New training methods will be proposed to further improve the NF controller in terms of training efficiency, convergence, and robustness to accommodate time-varying and nonlinear system conditions.

2. The experimental setup will be improved to model more complex dynamic conditions, including a different orientation setup, DC motor parameters, and output voltage saturation.

3. An AAR prototype will be developed and installed to the FuelBoss. The control manipulating system will be designed, fabricated, and implemented to the drogue.

4. Smart sensor systems will be developed to monitor the AAR procedures, record positional data of the drogue, and transmit the data wirelessly to the FuelBoss aircraft.

5. Flight tests will be undertaken to record the real flight data corresponding to different flight conditions, so as to improve the design and models, as well as to train the NF controller.

References

[1]   Northrop Grumman. (2007, Dec. 10). *Photo Release -- Northrop Grumman KC-30 tanker aerial refueling boom system successfully completes in-flight contact with an F-16 receiver aircraft.* [Online] Available: https://news.northropgrumman.com/news/releases/photo-release-northrop-grumman-kc-30-tanker-aerial-refueling-boom-system-successfully-completes-in-flight-contact-with-an-f-16-receiver-aircraft

[2]   CAF Air Refueling Team. (2018, Dec. 24). *Canadian Forces – Operation IMPACT: air to air refueling*. [Online] Available: https://www.youtube.com/watch?v=sEdSHSqOhvY

[3]   S. Lamarche, "The backbone of reach & power: Air-to-air refueling in the RCAF," M.S. thesis, Department of National Defence, Canadian Forces College, Toronto, ON, Canada, 2015.

[4]   The Department of National Defence. (2021, Jun. 6). *Operation IMPACT*. [Online] Available: https://www.canada.ca/en/department-national-defence/services/operations/military-operations/current-operations/operation-impact.html

[5]   S. Fridman. (2020, Sep. 12) *Refueling demo at AirShow London 2020.* [Online] Available: https://www.jetphotos.com/photo/10184045

[6]   A, Erickson, P. W. Richards, A. Chaturvedi, E. Knoblauch and S. McLaughlin, "Aeroelastic modeling of hose and drogue aerial refueling," *AIAA SciTech Forum*, 2019.

[7]   X. Dai, Z. -B. Wei, Q. Quan and K. -Y. Cai, "Hose-drum-unit modeling and control for probe-and-drogue autonomous aerial refueling," *IEEE Transactions on Aerospace and Electronic Systems*, vol. 56, no. 4, pp. 2779-2791, Aug. 2020.

[8]   W. B. Ribbens, F. Saggio, R. Wierenga, and M. Feldmann, "Dynamic modeling of an aerial refueling hose & drogue System," *25th AIAA Applied Aerodynamics Conference*, 2007.

[9]   N. Fezans and T. Jann, "Modeling and simulation for the automation of aerial refueling of military transport aircraft with the probe-and-drogue system," *AIAA Modeling and Simulation Technologies Conference*, 2017.

[10]   M. M. van Lith, H. G. Visser, and H. S. Hosseini, "Modeling an operations concept for commercial air-to-air refueling based on a vehicle routing problem formulation," *29th Congress of the International Council of the Aeronautical Sciences*, Sep. 2014.

[11]   R. Nangia, "Operations and aircraft design towards greener civil aviation using air-to-air refuelling," *The Aeronautical Journal*, vol. 110, no. 1113, pp. 705-721, Feb. 2016.

[12]   J. Eichler, "Dynamic analysis of an in-flight refueling system," *Journal of Aircraft*, vol. 15, no. 5, pp. 311-318, 1978.

[13]   K. Ro and J. W. Kamman, "Modeling and simulation of hose-paradrogue aerial refueling systems." *Journal of Guidance, Control, and Dynamics*, vol. 33, no. 1, pp. 53-63, 2010.

[14]   Y. Kuizhi, C. Liangliang Z. Tieying J. Jinzu and Y. Dazhao, "Numerical simulation of the aerodynamic influence of an aircraft on the hose-refueling system during aerial refueling operations," *Aerospace Science and Technology*, vol. 49, pp. 34-40, 2016.

[15]   J. L. Hansen, J. E. Murray and N. V. Campos. "The NASA Dryden AAR project: a flight test approach to an aerial refueling system," *AIAA Atmospheric Flight Mechanics Conference and Exhibit*, 2004.

[16]   M. J. Vachon, R. J. Ray and C. Calianno, "Calculated drag of an aerial refueling assembly through airplane performance analysis," *42nd AIAA Aerospace Sciences Meeting and Exhibit*, 2004.

[17]   A, Erickson, P. W. Richards, M. Mor, A. Chaturvedi, E. Knoblauch and S. McLaughlin, "Modeling of electric reeling systems in aerial refueling hose pods using Matlab/Simulink," *AIAA SciTech Forum*, 2020.

[18]   H. Wang, X. Dong, J. Xue and J. Liu, "Dynamic modeling of a hose-drogue aerial refueling system and integral sliding mode backstepping control for the hose whipping phenomenon," *Chinese Journal of Aeronautics,* vol. 27, no. 4, pp. 930-946, Mar. 2014.

[19]   C. D. Rahn, "Passive control," *Mechatronic Control of Distributed Noise and Vibration*, Berlin, Heidelberg: Springer, 2001.

[20]   T. T. Soong and G. F. Dargush, "Passive energy dissipation and active control," *Structural Engineering Handbook*, Boca Raton: CRC Press LLC, 1999.

[21]   N. Abe, "Passive and active switching vibration control with pendulum type damper," *Proceedings of the 2004 IEEE International Conference on Control Applications*, 2004, vol. 2, pp. 1037-1042.

[22]   Y. L. Xu and J. Teng, "Optimum design of active/passive control devices for tall buildings under earthquake excitation," *The Structural Design of Tall Buildings,* vol. 11, no. 2, pp. 109-127, Apr. 2001.

[23]   T. Roy and V. Matsagar, "Probabilistic assessment of steel buildings installed with passive control devices under multi-hazard scenario of earthquake and wind," *Structural Safety,* vol. 85, Jul. 2020.

[24]   I. G. Buckle, "Passive control of structures for seismic loads." *Special Issue on the 12th World Conference on Earthquake Engineering,* vol. 33, no. 3, pp. 209-221, Sep. 2000.

[25]   Y. Zhang, T. Schauer and A. Bleicher, "Optimized passive/semi-active vibration control using distributed-multiple tuned facade damping system in tall buildings," *Journal of Building Engineering,* vol. 52, Jul. 2022.

[26]   M.A. Johnson and M.H. Moradi, "PID control technology," *PID Control*, London, UK: Springer-Verlag London Limited, 2005.

[27]   M. -A. Bégin, R. Poon and I. Hunter, "Streamlined tuning procedure for stable PID control of flexible-base manipulators," *IEEE Robotics and Automation Letters*, vol. 6, no. 4, pp. 7413-7420, Oct. 2021.

[28]   Y. Guo and M. E. A. Mohamed, "Speed control of direct current motor using ANFIS based hybrid P-I-D configuration controller," *IEEE Access*, vol. 8, 2020.

[29]   Y. Liu and D. Sun, "Stabilizing a flexible beam handled by two manipulators via PD feedback," in *IEEE Transactions on Automatic Control*, vol. 45, no. 11, pp. 2159-2164, Nov. 2000.

[30]   M. Pourebrahim, M. Ayati and M. Mahjoob, "Design and implementation of PI and fuzzy PID supervisory controllers for a flexible link robot," *2nd International Conference on Control Science and Systems Engineering (ICCSSE)*, 2016, pp. 270-275.

[31]   J. Annisa, I. Z. M. Darus, M. O. Tokhi and S. Mohamaddan, "Implementation of PID based controller tuned by evolutionary algorithm for double link flexible robotic manipulator," *International Conference on Computational Approach in Smart Systems Design and Applications (ICASSDA)*, 2018, pp. 1-5.

[32]   N. Sheng, X. Chen, H. Ge and D. Li, "Optimal interval type 2 fuzzy PID controller and its application inverted pendulum system," *IEEE 2nd International Conference on Automation, Electronics and Electrical Engineering (AUTEEE)*, 2019, pp. 635-637.

[33]   K. Łapa and K. Cpałka, "Flexible fuzzy PID controller (FFPIDC) and a nature-inspired method for its construction," *IEEE Transactions on Industrial Informatics*, vol. 14, no. 3, pp. 1078-1088, Mar. 2018.

[34]   H. Bilal, W. Yao, Y. Guo, Y. Wu and J. Guo, "Experimental validation of fuzzy PID control of flexible joint system in presence of uncertainties," *36th Chinese Control Conference (CCC)*, 2017, pp. 4192-4197.

[35]   S. -Y. Han, J. -F. Dong, J. Zhou and Y. -H. Chen, "Adaptive fuzzy PID control strategy for vehicle active suspension based on road evaluation," *Electronics,* vol. 11, no. 6, Mar. 2022.

[36]   F. Gong, S. Nie, H. Ji, R. Hong, F. Yin and X. Yan, "Pipeline vibration control using magnetorheological damping clamps under fuzzy–PID control algorithm," *micromachines,* vol. 13, no. 4, Mar. 2022.

[37]   L. Cui, H. Wang, X. Liang, J. Wang and W. Chen, "Visual servoing of a flexible aerial refueling boom with an eye-in-hand camera," *IEEE Transactions on Systems, Man, and Cybernetics: Systems*, vol. 51, no. 10, pp. 6282-6292, Oct. 2021.

[38]   Y. Ling, Y. Li and J. Xiang, "Flexible generator: generation unit integrated by energy storage system and synchronous generator," *IEEE Transactions on Power Systems*, vol. 35, no. 6, pp. 4263-4271, Nov. 2020.

[39]   C. Edwards and S. Spurgeon, "Passive energy dissipation and active control," *Sliding Mode Control: Theory and Applications*, Taylor & Francis, 1998.

[40]   T. Long et al., "A vibration control method for hybrid-structured flexible manipulator based on sliding mode control and reinforcement learning," *IEEE Transactions on Neural Networks and Learning Systems*, vol. 32, no. 2, pp. 841-852, Feb. 2021.

[41]   K. Rsetam, Z. Cao and Z. Man, "Design of robust terminal sliding mode control for underactuated flexible joint robot," *IEEE Transactions on Systems, Man, and Cybernetics*, vol. 52, no. 7, pp. 4272-4285, Jul. 2022.

[42]   J. Li, J. Wang, H. Peng, Y. Hu and H. Su, "Fuzzy-torque approximation-enhanced sliding mode control for lateral stability of mobile robot," *IEEE Transactions on Systems, Man, and Cybernetics*, vol. 52, no. 4, pp. 2491-2500, April 2022.

[43]   S. Wang, L. Tao, Q. Chen, J. Na and X. Ren, "USDE-based sliding mode control for servo mechanisms with unknown system dynamics," *IEEE/ASME Transactions on Mechatronics*, vol. 25, no. 2, pp. 1056-1066, April 2020.

[44]   J. Rodriguez, M. Collet and S. Chesné, "Active vibration control on a smart composite structure using modal-shaped sliding mode control," *Journal of Vibration and Acoustics,* vol. 144, Apr. 2022.

[45]   I. D. Landau, R. Lozano, M. M'Saad and A. Karimi, "Introduction to adaptive control," *Adaptive Control: Algorithms, Analysis and Applications*, London: Springer, 2011.

[46]   S. Wang, H. Yu, J. Yu, J. Na and X. Ren, "Neural-network-based adaptive funnel control for servo mechanisms with unknown dead-zone," *IEEE Transactions on Cybernetics*, vol. 50, no. 4, pp. 1383-1394, April 2020.

[47]   C. Lijia, H. Xiaoxiang and G. Yang, "Robust adaptive backstepping control of UAV with lumped uncertainties," *International Conference on Mechatronics and Control (ICMC)*, 2014, pp. 961-965.

[48]   Y. -J. Liu, S. Lu, S. Tong, X. Chen, C. L. P. Chen, and D. -J. Li "Adaptive control-based Barrier Lyapunov Functions for a class of stochastic nonlinear systems with full state constraints," *Automatica*, vol. 87, pp. 83-93, Jan. 2018.

[49]   B. Song and J. K. Hedrick, "A brief history of dynamic surface control," *Dynamic Surface Control of Uncertain Nonlinear Systems: An LMI Approach*, London: Springer, 2011.

[50]   J. Huang, S. Ri, L. Liu, Y. Wang, J. Kim and G. Pak, "Nonlinear disturbance observer-based dynamic surface control of mobile wheeled inverted pendulum," *IEEE Transactions on Control Systems Technology*, vol. 23, no. 6, pp. 2400-2407, Nov. 2015.

[51]   Z. Peng, Y. Jiang and J. Wang, "Event-triggered dynamic surface control of an underactuated autonomous surface vehicle for target enclosing," *IEEE Transactions on Industrial Electronics*, vol. 68, no. 4, pp. 3402-3412, Apr. 2021.

[52]   F. O. Karray and C. de Silva, "Neuro-fuzzy Systems," *Soft Computing and Intelligent Systems Design: Theory, Tools and Applications*, London: Springer, 2011.

[53]   H. Li, L. Wang, H. Du and A. Boulkroune, "Adaptive fuzzy backstepping tracking control for strict-feedback systems with input delay," *IEEE Transactions on Fuzzy Systems*, vol. 25, no. 3, pp. 642-652, Jun. 2017.

[54]   Z. Li, C.-Y. Su, L. Wang, Z. Chen and T. Chai, "Nonlinear disturbance observer-based control design for a robotic exoskeleton incorporating fuzzy approximation," *IEEE Transactions on Industrial Electronics*, vol. 62, no. 9, pp. 5763-5775, Sep. 2015.

[55]   M. Li, H. Chen and R. Zhang, "An input dead zones considered adaptive fuzzy control approach for double pendulum cranes with variable rope lengths," *IEEE/ASME Transactions on Mechatronics,* 2021.

[56]   C. Sendi, "Attitude stabilization during retargeting maneuver of flexible spacecraft subject to time delay and actuators saturation," *IEEE Aerospace Conference*, 2020

[57]   Y. Ren, Z. Zhao, C. K. Ahn and H. -X. Li, "Adaptive fuzzy control for an uncertain axially moving slung-load cable system of a hovering helicopter with actuator fault," *IEEE Transactions on Fuzzy Systems,* 2021.

[58]   M. Aldawod, B. Samali, F. Naghdy and K. C. S. Kwok, "Active control of along wind response of tall building using a fuzzy controller," *Engineering Structures*, vol. 23, no. 11, pp. 1512-1522, Nov. 2001.

[59]   J. -S. R. Jang, C. -T. Sun and E. Mizutani, "Fuzzy Inference Systems," *Neuro-Fuzzy and Soft Computing: A Computational Approach to Learning and Machine Intelligence*, England: Pearson Education Limited, 2004.

[60]   S. Zhang, Y. Wu, X. He and J. Wang, "Neural network-based cooperative trajectory tracking control for a mobile dual flexible manipulator," *IEEE Transactions on Neural Networks and Learning Systems*, 2022.

[61]   H. Wang, X. Zhou and Y. Tian, "Robust adaptive fault-tolerant control using RBF-based neural network for a rigid-flexible robotic system with unknown control direction," *International Journal of Robust and Nonlinear Control,* vol. 32, no. 3, Feb. 2022.

[62]   S. Diao, W. Sun and S. -F. Se, "Neural-based adaptive event-triggered tracking control for flexible-joint robots with random noises," *International Journal of Robust and Nonlinear Control,* vol. 32, no. 5, Mar. 2022.

[63]   C. Sun, W. He and J. Hong, "Neural network control of a flexible robotic manipulator using the lumped spring-mass model," *IEEE Transactions on Systems, Man, and Cybernetics*, vol. 47, no. 8, pp. 1863-1874, Aug. 2017.

[64]   H. Gao, W. He, L. Zhang and C. Sun, "Neural-network control of a stand-alone tall building-like structure with an eccentric load: an experimental investigation," *IEEE Transactions on Cybernetics*, vol. 52, no. 6, pp. 4083-4094, Jun. 2022.
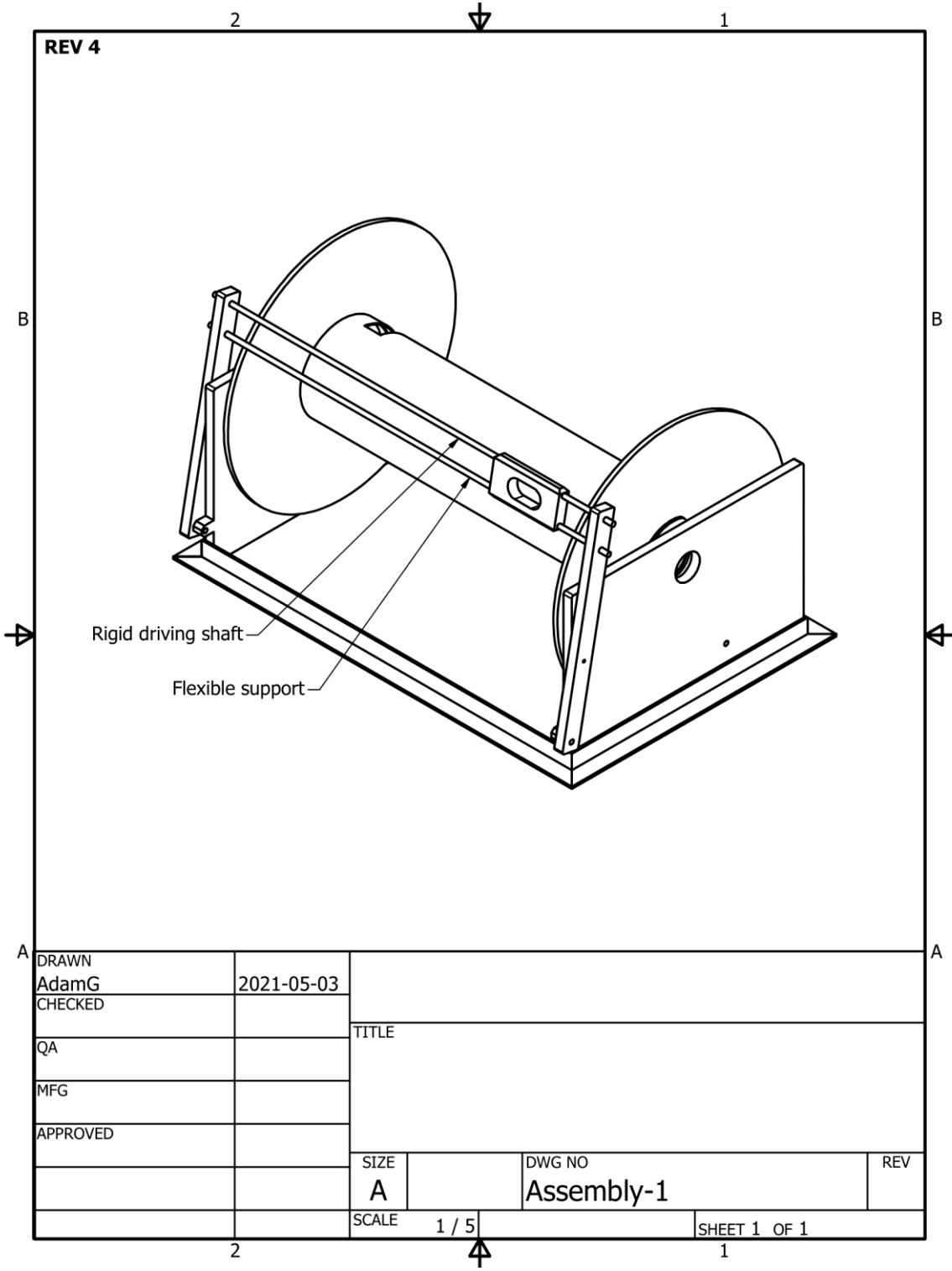
[65]   S. Zhang, P. Yang, L. Kong, W. Chen, Q. Fu and K. Peng, "Neural networks-based fault tolerant control of a robot via fast terminal sliding mode," *IEEE Transactions on Systems, Man, and Cybernetics*, Aug. 2019.

[66]   S. K.V. and G. N. Pillai, "Extreme learning ANFIS control of a flexible link manipulator," *14th IEEE India Council International Conference (INDICON)*, 2017

[67]   F. Junyao, X. Wenping and L. Guohai, "Vibration control for vehicle active suspension based on ANFIS method," *36th Chinese Control Conference (CCC)*, 2017

[68]   A. Dabiri, M. Nazari and E. A. Butcher, "Adaptive neural-fuzzy inference system to control dynamical systems with fractional order dampers," *American Control Conference (ACC)*, 2017.

[69]   X. Wang, S. M. Abtahi, M. Chahari and T. Zhao, "An adaptive neuro-fuzzy model for attitude estimation and control of a 3 DOF system," *Mathematics,* vol. 10, Mar. 2022.

[70]   J. Tavoosi and F. Mohammadi, "A new type-II fuzzy system for flexible-joint robot arm control," *6th International Conference on Control, Instrumentation and Automation (ICCIA)*, 2019, pp. 1-4.

[71]   I. Chawla and A. Singla, "Real-time control of a rotary inverted pendulum using robust LQR-based ANFIS controller," *Internal Journal of Nonlinear Sciences and Numerical Simulation,* vol. 19, no. 3, pp. 379-389, 2018.

[72]   A. Madkour, M. A. Hossain, K. P. Dahal and H. Yu, "Intelligent learning algorithms for active vibration control," *IEEE Transactions on Systems, Man, and Cybernetics*, vol. 37, no. 5, pp. 1022-1033, Sept. 2007.

[73]   S. Harifi, M. Khalilian, J. Mohammadzadeh and S. Ebrahimnejad, "Optimizing a neuro-fuzzy system based on nature-inspired emperor penguins colony optimization algorithm," *IEEE Transactions on Fuzzy Systems*, vol. 28, no. 6, pp. 1110-1124, Jun. 2020.

[74]   B. Selma, S. Chouraqui, B. Selma, H. Abouaïssa and T. Bakir, "Autonomous trajectory tracking of a quadrotor UAV using ANFIS controller based on Gaussian pigeon-inspired optimization," *CEAS Aeronautical Journal*., vol. 12, pp. 69-83, Oct. 2020.

[75]   M. Dorigo, V. Maniezzo and A. Colorni, "Ant system: optimization by a colony of cooperating agents," *IEEE Transactions on Systems, Man, and Cybernetics*, vol. 26, no. 1, pp. 29-41, Feb. 1996.

[76]   S. I. Purdy, "Probe and drogue aerial refueling systems," in *Encyclopedia of Aerospace Engineering*, Hoboken, NJ, USA: John Wiley & Sons, 2010.

[77]   FuelBoss. (2022). *Innovative Refueling*. [Online] Available: http://fuelboss.ca/innovation/

[78]   H. Huang, G. Tang, H. Chen, L. Han and D. Xie, "Dynamic modeling and vibration suppression for two-link underwater flexible manipulators," *IEEE Access*, vol. 10, 2022.

[79]   W. Zhu, Q. Zong and B. Tian, "Adaptive tracking and command shaped vibration control of flexible spacecraft," *IET Control Theory and Applications*, vol. 13, no. 8, pp. 1121-1128, May 2019.

[80]   C. F. Cutforth and L. Y. Pao, "Adaptive input shaping for maneuvering flexible structures," *Automatica*, vol. 40 no. 4, pp. 685-693, Apr. 2004.

[81]   North Atlantic Treaty Organization (NATO), *ATP-56(A) air to air refueling*, AJP 3.3.4.2, Nov. 2000.

[82]   Product brochure: Cobham Mission Equipment, *Wing air refueling pod: 34" series*, ADV10602, 2009.

[83]   Product brochure: Cobham Mission Equipment, *Probes: fixed, telescopic and actuated probes*, V7, Dec. 2019.

[84]   North Atlantic Treaty Organization (NATO), *NATO STANAG 3447, Air-to-air (aerial) refueling equipment: probe-drogue interface characteristics,* Jun. 2016.

[85]   Product brochure: Cobham Mission Equipment, *FR600: fuselage refueling unit*, ADV10603, 2009.

[86]   Department of Defence, *Couplings, regulated, aerial pressure refueling type MA-2, type MA-3 and type MA-4,* MIL-PRF-81975C amendment 2, Oct. 2013.

[87]   Department of the Navy, Bureau of Naval Weapons, *General specification for air refueling systems*, MIL-A-19736A amendment 2, Mar. 1966.

[88]   North Atlantic Treaty Organization (NATO), *NATO STANAG 3971, Air-to-air refueling,* Apr. 2019.

[89]   Y. Krispin and M. Velger, "Controllable hose-and-drogue in-flight refueling system," U.S. Patent 5 326 052, Jul. 5, 1994.

[90]   F. Saggio III, W. B. Ribbens and K. K. Ooi, "Stabilization of a drogue body," U.S. Patent 6 994 294, Feb. 7, 2006.

[91]   D. A. Pruzan and D. J. Lesieutre, "Drogue control systems and apparatus," U.S. Patent 10 703 501 B2, Jul. 7, 2020.

[92]   T. Kuk, "Active control of aerial refueling drogue," Ph.D. dissertation, Department of Mechanical Engineering, Western Michigan University, Kalamazoo, MI, USA, 2014.

[93]   Y. Song, W. He, X. He and Z. Han, "Vibration control of a high-rise building structure: theory and experiment," *IEEE/CAA Journal of Automatica Sinica*, vol. 8, no. 4, pp. 866-875, Apr. 2021.

[94]   H. Gao, W. He, Y. Zhang and C. Sun, "Vibration control based on reinforcement learning for a flexible building-like structure system with active mass damper against disturbance effects," *59th IEEE Conference on Decision and Control (CDC)*, 2020, pp. 2380-2385.

[95]   Air Tractor Inc., private communication, Apr. 29, 2022.

[96]   User manual: Quanser Consulting Inc., Smart *Structure User Manual,* Revision 2.2, n.d.

[97]   User manual: Quanser Consulting Inc., *Universal Power Module User Manual,* Revision 2.0, n.d.

[98]   Quanser Consulting Inc. (2019, Oct. 25). *Quanser HIL SDK*. [Online] Available: https://github.com/quanser/hil_sdk_win64

[99]   User manual: Quanser Consulting Inc., *Q4 data acquisition system user's guide,* version 1.0, 2003.

[100]   R. Frank, *Understanding Smart Sensors*, Boston, MA, United States: Artech House, 2013.

[101]   J. McAlorum, T. Rubert, G. Fusiek, I. McKeeman, L. Clayburn, M. Perry and P. Niewczas, "Comparison of epoxy and braze-welded attachment methods for FBG strain gauges," *IEEE SENSORS*, 2017.

[102]   W. Wang, "An intelligent system for machinery condition monitoring," *IEEE Transactions in Fuzzy Systems*, vol. 16, no. 1, pp. 110-122, Feb. 2008.

[103]   S. G. Kelly, *Mechanical Vibrations: Theory and applications*, Australia: Cengage Learning, 2012.

[104]   M. S. Allen, H. Sumali and D. S. Epp "Piecewise-linear restoring force surfaces for semi-nonparametric identification of nonlinear systems," in *Nonlinear Dynamics*, vol. 54, pp. 123-135, 2008.

[105] K. B. Peterson and M. S. Pederson, *The Matrix Cookbook,* Technical University of
Denmark, Nov. 15, 2012.

Appendix A:
Preliminary Hose Drum Unit Design

REV 4

B | B

Rigid driving shaft

Flexible support

DRAWN					
AdamG	2021-05-03				
CHECKED					
		TITLE			
QA					
MFG					
APPROVED					
		SIZE	DWG NO		REV
		A	Assembly-1		
		SCALE 1 / 5		SHEET 1 OF 1	

A1

REV 4

14 1/4

16 1/4

B

24 1/2

B

DRAWN					
AdamG	2021-05-03				
CHECKED					
QA		TITLE			
MFG					
APPROVED					
		SIZE		DWG NO	REV
		A		Assembly-2	
		SCALE	1 / 8	SHEET 1 OF 1	

Appendix B:
Euler-Lagrange Differentiation

Consider the total kinetic energy of the flexible system from Equation (3.16):

$$T = \frac{1}{2}m_b\dot{x}_b^2 + \frac{1}{2}J_p\dot{\theta}_p^2 + \frac{1}{2}m_p\left(\left(\dot{\theta}_p\cos(\theta_p)\ell_p + \dot{x}_b\right)^2 + \left(\dot{\theta}_p\sin(\theta_p)\ell_p\right)^2\right) \tag{B.1}$$

Consider the total potential energy of the flexible system from Equation (3.6):

$$V = m_p g\left(\cos\theta_p\right)\ell_p + \frac{1}{2}k_s x_b^2 \tag{B.2}$$

Now consider the Lagrangian of the system, which has the following form:

$$\frac{\partial}{\partial t}\left(\frac{\partial T}{\partial \dot{q}_i}\right) - \left(\frac{\partial T}{\partial q_i}\right) + \left(\frac{\partial V}{\partial q_i}\right) = Q_i \tag{B.3}$$

For $i = 1$, $q_1 = x_b$:

$$\left(\frac{d}{dt}\right)\left(\frac{\partial T}{\partial \dot{x}_b}\right) = \left(\frac{d}{dt}\right)\left[\frac{1}{2}m_b\dot{x}_b(2) + \frac{1}{2}m_p\left(\left(\dot{\theta}_p\cos(\theta_p)\ell_p + \dot{x}_b\right)(2)\right)\right] \tag{B.4}$$

$$\left(\frac{d}{dt}\right)\left(\frac{\partial T}{\partial \dot{x}_b}\right) = \left(\frac{d}{dt}\right)\left[m_b\dot{x}_b + m_p\dot{\theta}_p\cos(\theta_p)\ell_p + m_p\dot{x}_b\right] \tag{B.5}$$

$$\left(\frac{d}{dt}\right)\left(\frac{\partial T}{\partial \dot{x}_b}\right) = \left(\frac{d}{dt}\right)\left[(m_b + m_p)\dot{x}_b + m_p\dot{\theta}_p\cos(\theta_p)\ell_p\right] \tag{B.6}$$

Consider the product rule, where $(uv)' = u'v + uv'$:

$$\left(\frac{d}{dt}\right)\left(\frac{\partial T}{\partial \dot{x}_b}\right) = (m_b + m_p)\ddot{x}_b + m_p\ddot{\theta}_p\cos(\theta_p)\ell_p - m_p\dot{\theta}_p\dot{\theta}_p\sin(\theta_p)\ell_p \tag{B.7}$$

$$\left(\frac{d}{dt}\right)\left(\frac{\partial T}{\partial \dot{x}_b}\right) = (m_b + m_p)\ddot{x}_b + m_p\ell_p\cos(\theta_p)\ddot{\theta}_p - m_p\ell_p\sin(\theta_p)\dot{\theta}_p^2 \tag{B.8}$$

Further:

$$\left(\frac{\partial T}{\partial x_b}\right) = 0 \tag{B.9}$$

$$\left(\frac{\partial V}{\partial x_b}\right) = \frac{1}{2}k_s x_b(2) = k_s x_b \tag{B.10}$$

B1

Substituting Equations (B.8)-(B.10) into Equation (B.3) yields:

$$\left(m_b + m_p\right)\ddot{x}_b + m_p\ell_p \cos(\theta_p)\ddot{\theta}_p - m_p\ell_p \sin(\theta_p)\dot{\theta}_p^2 + k_s x_b = Q_1 \tag{B.11}$$

For $i = 2$, $q_2 = \theta_p$:

$$\left(\frac{d}{dt}\right)\left(\frac{\partial T}{\partial\dot{\theta}_p}\right) = \left(\frac{d}{dt}\right)\left[\frac{1}{2}J_p\dot{\theta}_p(2)\right.$$
$$+ \frac{1}{2}m_p\left((\dot{\theta}_p\cos(\theta_p)\ell_p + \dot{x}_b)(2)\cos(\theta_p)\ell_p \right. \tag{B.12}$$
$$\left.+ (\dot{\theta}_p\sin(\theta_p)\ell_p)(2)(\sin(\theta_p)\ell_p)\right)\Big]$$

$$\left(\frac{d}{dt}\right)\left(\frac{\partial T}{\partial\dot{\theta}_p}\right) = \left(\frac{d}{dt}\right)\left[J_p\dot{\theta}_p + m_p\dot{\theta}_p\cos^2(\theta_p)\ell_p^2 + m_p\dot{x}_b\cos(\theta_p)\ell_p\right.$$
$$\left. + m_p\dot{\theta}_p\sin^2(\theta_p)\ell_p^2\right] \tag{B.13}$$

$$\left(\frac{d}{dt}\right)\left(\frac{\partial T}{\partial\dot{\theta}_p}\right) = \left(\frac{d}{dt}\right)\left[J_p\dot{\theta}_p + m_p\dot{x}_b\cos(\theta_p)\ell_p + m_p\dot{\theta}_p\ell_p^2(\sin^2(\theta_p) + \cos^2(\theta_p))\right] \tag{B.14}$$

Consider:

$$\sin^2(\theta_p) + \cos^2(\theta_p) = 1 \tag{B.15}$$

Then:

$$\left(\frac{d}{dt}\right)\left(\frac{\partial T}{\partial\dot{\theta}_p}\right) = \left(\frac{d}{dt}\right)\left[J_p\dot{\theta}_p + m_p\dot{x}_b\cos(\theta_p)\ell_p + m_p\dot{\theta}_p\ell_p^2\right] \tag{B.16}$$

Using the product rule:

$$\left(\frac{d}{dt}\right)\left(\frac{\partial T}{\partial\dot{\theta}_p}\right) = J_p\ddot{\theta}_p + m_p\ddot{\theta}_p\ell_p^2 + m_p\cos(\theta_p)\ell_p\ddot{x}_b - m_p\dot{x}_b\dot{\theta}_p\sin(\theta_p)\ell_p \tag{B.17}$$

$$\left(\frac{d}{dt}\right)\left(\frac{\partial T}{\partial\dot{\theta}_p}\right) = (J_p + m_p\ell_p^2)\ddot{\theta}_p + m_p\cos(\theta_p)\ell_p\ddot{x}_b - m_p\dot{x}_b\dot{\theta}_p\sin(\theta_p)\ell_p \tag{B.18}$$

Further:

$$\left(\frac{\partial T}{\partial \theta_b}\right) = \frac{1}{2}m_p \left(\left(\dot{\theta}_p \cos(\theta_p)\,\ell_p + \dot{x}_b\right)(2)\dot{\theta}_p \sin(\theta_p)\,\ell_p(-1) \right.$$
$$\left. + \left(\dot{\theta}_p \sin(\theta_p)\,\ell_p\right)(2)\left(\dot{\theta}_p \cos(\theta_p)\,\ell_p\right) \right) \tag{B.19}$$

$$\left(\frac{\partial T}{\partial \theta_b}\right) = -m_p \ell_p^2 \dot{\theta}_p^2 \sin(\theta_p)\cos(\theta_p) + m_p \ell_p^2 \dot{\theta}_p^2 \sin(\theta_p)\cos(\theta_p)$$
$$- m_p \dot{x}_b \dot{\theta}_p \sin(\theta_p)\,\ell_p \tag{B.20}$$

Simplifying Equation (B.20) results in:

$$\left(\frac{\partial T}{\partial \theta_b}\right) = -m_p \dot{x}_b \dot{\theta}_p \sin(\theta_p)\,\ell_p \tag{B.21}$$

$$\left(\frac{\partial V}{\partial \theta_p}\right) = -m_p g \sin(\theta_p)\,\ell_p \tag{B.22}$$

Substituting Equations (B.18), (B.21) and (B.22) into Equation (B.3) yields:

$$\left(J_p + m_p \ell_p^2\right)\ddot{\theta}_p + m_p \cos(\theta_p)\,\ell_p \ddot{x}_b - m_p g \sin(\theta_p)\,\ell_p = Q_2 \tag{B.23}$$

Appendix C:

General Forms of Vector Derivatives

Consider two column vectors $\mathbf{x}, \mathbf{y} \in \mathbb{R}^n$, and the following scalar function :

$$f(\mathbf{x}) = \mathbf{x}^T\mathbf{y} \tag{C.1}$$

Consider that a transpose of a scalar is itself, then Equation (C.1) can also be written as:

$$f(\mathbf{x}) = \mathbf{y}^T\mathbf{x} \tag{C.2}$$

From [101], the following general cases apply for vector derivatives

$$\frac{\partial(\mathbf{x}^T\mathbf{y})}{\partial\mathbf{x}} = \frac{\partial(\mathbf{y}^T\mathbf{x})}{\partial\mathbf{x}} = \mathbf{y} \tag{C.3}$$

Similarly:

$$\frac{\partial(\mathbf{x}^T\mathbf{x})}{\partial\mathbf{x}} = 2\mathbf{x} \tag{C.4}$$

$$\frac{\partial(\mathbf{y}^T\mathbf{y})}{\partial\mathbf{x}} = 0 \tag{C.5}$$

Consider matrix $\mathbf{A} \in \mathbb{R}^{n \times n}$, then:

$$\frac{\partial(\mathbf{x}^T\mathbf{A})}{\partial\mathbf{x}} = \frac{\partial(\mathbf{A}^T\mathbf{x})}{\partial\mathbf{x}} = \mathbf{A} \tag{C.6}$$

$$\frac{\partial(\mathbf{x}^T\mathbf{A}\mathbf{y})}{\partial\mathbf{x}} = \frac{\partial(\mathbf{y}^T\mathbf{A}^T\mathbf{x})}{\partial\mathbf{x}} = \mathbf{A}\mathbf{y} \tag{C.7}$$

$$\frac{\partial(\mathbf{y}^T\mathbf{A}\mathbf{x})}{\partial\mathbf{x}} = \frac{\partial(\mathbf{x}^T\mathbf{A}^T\mathbf{y})}{\partial\mathbf{x}} = \mathbf{A}^T\mathbf{y} \tag{C.8}$$

$$\frac{\partial(\mathbf{x}^T\mathbf{A}\mathbf{x})}{\partial\mathbf{x}} = \frac{\partial(\mathbf{x}^T\mathbf{A}^T\mathbf{x})}{\partial\mathbf{x}} = (\mathbf{A} + \mathbf{A}^T)\mathbf{x} \tag{C.9}$$

$$\frac{\partial(\mathbf{y}^T\mathbf{A}\mathbf{y})}{\partial x} = \frac{\partial(\mathbf{y}^T\mathbf{A}^T\mathbf{y})}{\partial x} = 0 \tag{C.10}$$

Note that if $\mathbf{A}$ is constant matrix then Equation (C.9) becomes:

$$\frac{\partial(\mathbf{x}^T\mathbf{A}\mathbf{x})}{\partial\mathbf{x}} = \frac{\partial(\mathbf{x}^T\mathbf{A}^T\mathbf{x})}{\partial\mathbf{x}} = 2\mathbf{A}\mathbf{x} \tag{C.11}$$

Appendix D:
Experimental Data Sets

The full experimental results corresponding to different loading conditions are listed in Tables D.1-D.4.

Table D.1: Full experimental results, no additional mass blocks.

Trial	Controller	Overshoot (cm)	Undershoot (cm)	Settling Time (msec)
1	Controller-1	9.55	3.58	389
	Controller-2	6.80	1.41	269
	Controller-3	7.20	1.76	260
	Controller-4	6.59	0.75	263
2	Controller-1	9.50	3.57	411
	Controller-2	7.10	1.58	363
	Controller-3	7.09	1.65	262
	Controller-4	6.65	0.77	263
3	Controller-1	9.47	3.52	411
	Controller-2	7.04	1.55	362
	Controller-3	6.94	1.58	317
	Controller-4	6.62	0.82	298
4	Controller-1	9.54	3.56	310
	Controller-2	7.02	1.61	352
	Controller-3	6.98	1.62	261
	Controller-4	6.64	0.76	263
5	Controller-1	9.67	3.58	399
	Controller-2	7.04	1.55	306
	Controller-3	6.99	1.66	260
	Controller-4	6.64	0.79	298
6	Controller-1	9.30	3.64	455
	Controller-2	7.14	1.57	270
	Controller-3	6.94	1.58	270
	Controller-4	6.60	0.78	300

Table D.2: Full experimental results, additional mass blocks on Zone 1.

Trial	Controller	Overshoot (cm)	Undershoot (cm)	Settling Time (msec)
1	Controller-1	8.88	3.12	278
	Controller-2	6.47	0.90	238
	Controller-3	6.47	1.03	189
	Controller-4	6.35	0.89	206
2	Controller-1	8.90	3.09	233
	Controller-2	6.55	0.99	229
	Controller-3	6.42	1.03	189
	Controller-4	6.30	0.82	215
3	Controller-1	8.83	3.07	236
	Controller-2	6.71	1.11	230
	Controller-3	6.49	0.93	189
	Controller-4	6.22	0.82	189
4	Controller-1	8.94	3.24	234
	Controller-2	6.56	1.02	237
	Controller-3	6.53	1.00	225
	Controller-4	6.28	0.90	189
5	Controller-1	8.93	3.19	238
	Controller-2	6.70	1.03	228
	Controller-3	6.43	1.08	224
	Controller-4	6.34	0.86	190
6	Controller-1	8.82	3.14	278
	Controller-2	6.64	1.09	229
	Controller-3	6.50	1.07	214
	Controller-4	6.30	0.85	190

Table D.3:Full experimental results, additional mass blocks on Zone 2.

Trial	Controller	Overshoot (cm)	Undershoot (cm)	Settling Time (msec)
1	Controller-1	8.90	3.33	235
	Controller-2	6.86	0.96	262
	Controller-3	6.65	1.16	222
	Controller-4	6.45	0.85	223
2	Controller-1	8.91	3.34	271
	Controller-2	6.98	1.01	225
	Controller-3	6.66	1.13	212
	Controller-4	6.47	0.82	214
3	Controller-1	8.90	3.23	271
	Controller-2	6.94	0.98	226
	Controller-3	6.68	1.10	213
	Controller-4	6.47	0.79	215
4	Controller-1	8.99	3.33	272
	Controller-2	6.96	0.99	224
	Controller-3	6.70	1.18	212
	Controller-4	6.50	0.80	215
5	Controller-1	8.98	3.24	232
	Controller-2	6.90	0.88	262
	Controller-3	6.79	1.14	248
	Controller-4	6.44	0.78	215
6	Controller-1	8.94	3.29	270
	Controller-2	6.96	0.92	272
	Controller-3	6.66	1.13	222
	Controller-4	6.42	0.83	213

Table D.4:Full experimental results, additional mass blocks on Zone 3.

Trial	Controller	Overshoot (cm)	Undershoot (cm)	Settling Time (msec)
1	Controller-1	9.01	3.86	283
	Controller-2	6.90	1.01	262
	Controller-3	6.99	1.24	269
	Controller-4	6.72	0.93	214
2	Controller-1	9.02	3.60	270
	Controller-2	7.13	0.97	262
	Controller-3	7.08	1.15	259
	Controller-4	6.79	0.94	180
3	Controller-1	9.10	3.71	271
	Controller-2	7.03	1.00	263
	Controller-3	7.03	1.13	213
	Controller-4	6.63	0.91	204
4	Controller-1	9.13	3.74	272
	Controller-2	7.14	1.04	262
	Controller-3	7.01	1.15	212
	Controller-4	6.73	0.89	204
5	Controller-1	9.03	3.55	282
	Controller-2	7.12	1.05	262
	Controller-3	7.03	1.13	213
	Controller-4	6.68	0.87	204
6	Controller-1	9.03	3.71	282
	Controller-2	7.09	1.11	263
	Controller-3	7.03	1.16	214
	Controller-4	6.67	0.90	230

The average experimental results corresponding to different loading conditions are listed in Tables D.5-D.8.

Table D.5: Average experimental results, no additional mass blocks.

Controller	Overshoot (cm)	Undershoot (cm)	Settling Time (msec)
Controller-1	9.51	3.58	395.83
Controller-2	7.02	1.55	320.33
Controller-3	7.02	1.64	271.67
Controller-4	6.62	0.78	280.83

Table D.6: Average experimental results, additional mass blocks on Zone 1.

Controller	Overshoot (cm)	Undershoot (cm)	Settling Time (msec)
Controller-1	8.88	3.14	249.50
Controller-2	6.61	1.02	231.83
Controller-3	6.47	1.02	205.00
Controller-4	6.30	0.86	196.50

Table D.7: Average experimental results, additional mass blocks on Zone 2.

Controller	Overshoot (cm)	Undershoot (cm)	Settling Time (msec)
Controller-1	8.94	3.29	258.50
Controller-2	6.93	0.96	245.17
Controller-3	6.69	1.14	221.50
Controller-4	6.46	0.81	215.83

Table D.8: Average experimental results, additional mass blocks on Zone 3.

Controller	Overshoot (cm)	Undershoot (cm)	Settling Time (msec)
Controller-1	9.05	3.70	276.67
Controller-2	7.07	1.03	262.33
Controller-3	7.03	1.16	230.00
Controller-4	6.70	0.91	206.00